

SERGEI VLASSOV

Investigation of
nanoscale interactions and mechanical
properties of nanostructures using quartz
tuning fork based real-time
measurements



TARTU UNIVERSITY PRESS

The study was carried out in the Institute of Physics, University of Tartu

The dissertation was admitted on April 29, 2011 in partial fulfillment of the requirements for the degree of Doctor of Philosophy (material science), and allowed for defense by the Council of the Institute of Physics, University of Tartu.

Supervisor: Dr. Rünno Lõhmus, Institute of Physics, University of Tartu

Opponents: Ass. Prof. Ion Marius Sivebæk, Department of Mechanical Engineering, Technical University of Denmark, Denmark

Dr. Valdek Mikli, Tallinn University of Technology,
Faculty of Chemical and Materials Technology,
Centre for Materials Research

Defense: July 4, 2011, at the University of Tartu, Tartu; Estonia

This work has been supported by graduate school “Functional materials and processes” receiving funding from the European Social Fund under project 1.2.0401.09-0079 in Estonia.



ISSN 2228–0928

ISBN 978–9949–19–693–7 (trükis)

ISBN 978–9949–19–694–4 (PDF)

Autoriõigus: Sergei Vlassov, 2011

Tartu Ülikooli Kirjastus

www.tyk.ee

Tellimus nr. 351

CONTENTS

LIST OF ORIGINAL PUBLICATIONS	6
ABBREVIATIONS	8
PREFACE	9
1. QUARTZ TUNING FORK	11
2. ATOMIC FORCE MICROSCOPY – GENERAL DESCRIPTION AND TIP CONTAMINATION PROBLEM	21
3. NANOTRIBOLOGY AND MANIPULATION OF NANOSTRUCTURES	28
4. STRUCTURAL PROPERTIES OF NANOPARTICLES	32
5. AIMS OF THE STUDY	36
6. RESULTS AND DISCUSSION	37
6.1. Applications of QTF in mass, biological and chemical sensing (paper V and patent VII)	37
6.2. Real-time manipulation of gold nanoparticles inside scanning electron microscope with simultaneous force measurement (Paper I)	41
6.3. Real-time measurements of frictional and mechanical properties on ZnO nanowires inside SEM (Paper VI)	52
6.4. Crystal mismatched layers in pentagonal nanorods and nano- particles (Papers II and III)	58
6.5. Method of cleaning the tip of atomic force microscopy (Patent IV). ..	60
SUMMARY AND CONCLUSION	62
SUMMARY IN ESTONIAN	64
REFERENCES	66
ACKNOWLEDGEMENTS	71
PUBLICATIONS	73

LIST OF ORIGINAL PUBLICATIONS

- I. Vlassov, S; Polyakov, B; Dorogin, L; Lõhmus, A; Romanov, A; Kink, I; Gnecco, E; Lõhmus, R (2011). Real-time manipulation of gold nanoparticles inside a scanning electron microscope. Solid State Communications, 151, 688–692.
- II. Dorogin, L.; Vlassov, S.; Kolesnikova, A.; Kink, I.; Lõhmus, R.; Romanov, A. (2010). Crystal mismatched layers in pentagonal nanorods and nanoparticles. Physica Status Solidi B, 247 (2), 288–298.
- III. Dorogin, L.; Vlassov, S.; Kolesnikova, A.; Kink, I.; Lõhmus, R.; Romanov, A. (2010). Pentagonal Nanorods and Nanoparticles with Mismatched Shell Layers. Journal of Nanoscience and Nanotechnology, 10 (10), 6136–6143.

Patents:

- IV. Invention: Method for cleaning the atomic force microscope tip and the sample; Owner: Estonian Nanotechnology Competence Centre, University of Tartu; Authors: Sergei Vlassov, Ants Lõhmus, Rünno Lõhmus, Ilmar Kink, Jevgeni Šulga; Priority number: P200700031; Priority date: 12.06.2007

Submitted:

- V. S. Vlassov, O. Scheler, M. Plaado, R. Lõhmus, A. Kurg, K. Saal and I. Kink; Integrated carbon nanotube fiber–quartz tuning fork biosensor
- VI. B. Polyakov, L. Dorogin, S. Vlassov, I. Kink, A. Lohmus, R. Lohmus, Real-time measurements of frictional and mechanical properties on ZnO nanowires inside SEM
- VII. Invention: Method and device for measuring the chemical and biological analyte or viscosity and surface tension of the liquid; Owner: Estonian Nanotechnology Competence Centre, University of Tartu; Authors: Sergei Vlassov, Kristjan Saal, Rünno Lõhmus, Margo Plaado, Ants Lõhmus, Ilmar Kink; Priority number: P200900061; Priority date: 12.08.2009

Author's contribution

- Paper I: the author participated in development of experimental equipment, in experiments and data processing. Responsible for composing the manuscript.

Paper II and III: responsible for synthesis of nanoparticles. Participated in preparation of manuscript.

Paper V: the author is responsible for experimental equipment, all measurements and data processing.

Paper VI: author participated in development of experimental equipment, in experiments, and composition of manuscript.

Inventions IV and VII: the author is responsible for essence of invention, for claim formulation, for tenor, and for testing of the prototype.

ABBREVIATIONS

AFM	atomic force microscopy
BSA	bovine serum albumin
CNT	carbon nanotube
DSP	digital signal processing
DDS	direct data synthesis
FET	field-effect transistors
fcc	face centered cubic
FIB	focused ion beam
MEMS	microelectromechanical systems
NEMS	nanoelectromechanical systems
NP	nanoparticle
NW	nanowire
PLL	phase locked loop
SEM	scanning electron microscope
SET	single electron transistor
SPM	scanning probe microscopy
TEM	transmission electron microscope
QTF	quartz tuning fork
SNOM	scanning near field optical microscopy
SQUID	superconducting quantum interference device

PREFACE

The thesis is related to several important research fields – nanotribology, nanomechanics and biosensing – and can thus be considered multidisciplinary. However, there are strong links between the topics and every part contributes to a common ultimate goal – investigation of the interactions, behavior and the mechanical properties of materials at nanoscale.

From the technical side, the “kingpin” connecting most parts of the thesis is the quartz tuning fork (QTF), considered here in terms of high-resolution sensing for various scientific applications. In the results section of the thesis, the use of QTF in combination with nanoporous carbon nanotube (CNT) fiber for the development of the novel method and appropriate device for sensing the mass of adsorbed media in liquid as small as nanograms is proposed. Its application in tracking adsorption rate of protein on nanotubes is successfully demonstrated. Another application of QTF presented in the thesis is the force sensor for real-time measurements of the frictional and mechanical properties of gold nanoparticles (NPs) and ZnO nanowires (NWs) manipulated on a flat surface inside the scanning electron microscope.

In addition to the experimental measurements, the nanoparticles are also treated theoretically. New mechanism of stress relaxation in pentagonal nanorods and nanoparticles is proposed.

Moreover, a novel method of cleaning an atomic force microscopy tip – essential part of the sensor in the above-mentioned manipulation experiments – is elaborated.

For convenience, the connections between the research topics within the dissertation are presented schematically in Figure A.

The thesis is divided into 6 chapters. In the first chapter, the construction and operation principle of QTF are described. A brief introduction to the quartz crystal based sensing is given. The second chapter provides basic introduction to AFM and the tip contamination problem. The use of QTF in AFM is considered. The third chapter is dedicated to the controlled manipulation of nanostructures and its importance in terms of nanotribology and nanomechanics. In the fourth chapter, the main structural properties of gold nanoparticles, which are treated both experimentally and theoretically in the results section, are presented. The fifth chapter defines the aims of the present study. In chapter six, the essential results are described.

The work was performed mainly at the Institute of Physics, University of Tartu. A significant contribution in development of biosensing method was added by the Institute of Molecular and Cell Biology, Estonian Biocentre.

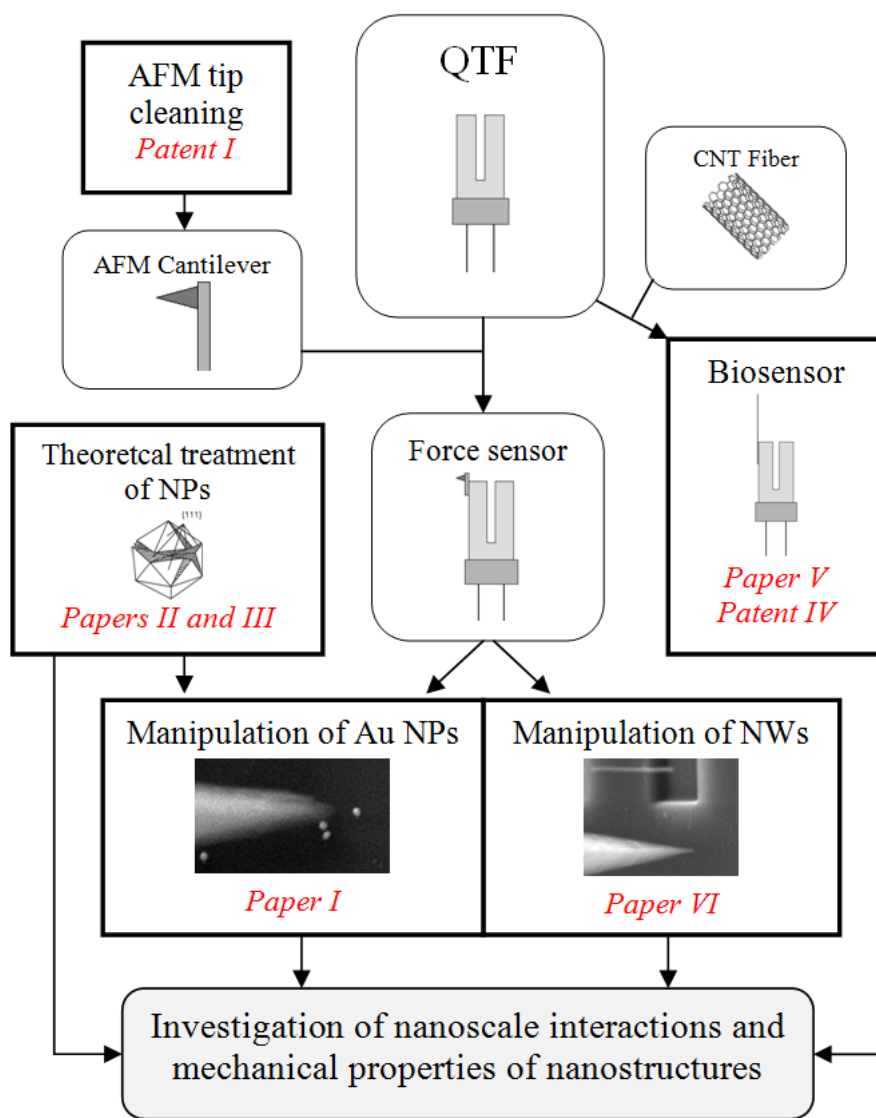


Figure A. Connections between topics of the thesis

BACKGROUND

I. Quartz Tuning Fork

I.1. Structure and operation principle

I.1.1. Tuning Fork

The tuning fork is one of the best mechanical oscillators. It was invented in 1711 by the English trumpeter John Share. The important mode of the tuning fork is the one where the two prongs oscillate in a mirrored fashion [1]. This has the unique advantage that the center of mass stays at rest and all forces are compensated inside the material connecting the two prongs.

I.1.2. Quartz Tuning Fork – general information

Quartz tuning fork (QTF) (fig. 1a) is a fork-shaped quartz crystal with thin-film metal electrodes deposited on both sides of the QTF beams. Since quartz is a piezoelectric material, QTF can oscillate laterally under applied ac voltage. Furthermore, the piezoelectric effect allows exciting and detecting the oscillation parameters (frequency, amplitude and phase) simultaneously.

The quality factor (Q-factor) is a fundamental quantity for characterizing the behavior of the resonator under the influence of external perturbing forces. It is defined as the ratio of the energy stored in the resonator to the energy loss during each oscillation period [1]. Due to the symmetrical shape and the fact that quartz is one of the materials with the lowest internal mechanical losses, Q-factor of QTF is very high – up to 100 000 in vacuum and 10 000 in air. [2].

Assuming the properties of QTF to be isotropic and neglecting the influence of the electrodes, the resonance frequency of QTF can be estimated from its mechanical parameters from simple relation [3]:

$$f_0 = \frac{1}{2\pi} \sqrt{\frac{3E_q I}{m_{\text{eff}} l^3}} \quad (1.1.2.1)$$

Here, I is the moment of inertia ($I = \omega t^3/12$ for rectangular cross-section), E_q is the Young's modulus of quartz ($7.87 \times 10^{10} \text{ N m}^{-2}$) and l , ω and t are the length, width and thickness of the cantilever, as shown in Fig.1b. m_{eff} is the effective mass for the oscillation beam, which is related to the real mass, m , through $m_{\text{eff}} = 0.2429m$ [4]. The resonant frequency of the most commercially available QTFs is 32.768 kHz (2^{15} Hz). More detailed theory is given in section 1.2.

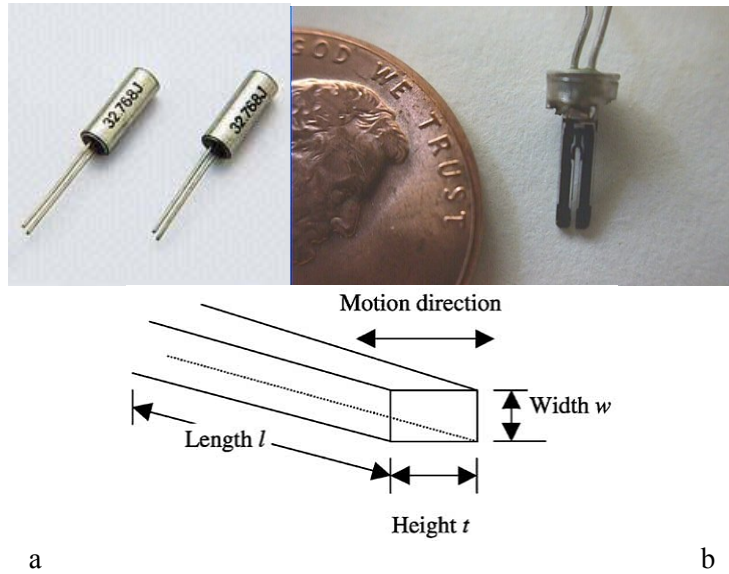


Figure 1. A photograph of the (a) encapsulated and (b) bare QTF; (c) a schematic diagram of the QTF beam.

QTF is mainly used as a frequency standard in various electronics and electro-mechanical systems. E.g. in a quartz watch, the fork is kept vibrating by an oscillator circuit which supplies voltage to the QTF electrodes. The quartz crystal itself is a capacitive component of that oscillator circuit. The alternating voltage of this circuit is detected, and then divided electronically to become a 1Hz signal, which is used to drive a stepper motor. Other applications are gyroscopes, microbalances, and various sensors, discussed in more details below. Due to the large industrial production QTFs are available at very low cost.

1.2. Theory of QTF

QTF is an electromechanical oscillator and its properties and behavior can be modeled using either electrical or mechanical approach. [5]. Main ideas are given below.

1.2.1. Electrical model

Piezoelectric oscillators can be modeled by an electronic equivalent circuit called the Butterworth-Van Dyke circuit (fig. 2) [6, 7]. The LRC resonator models the mechanical resonance: the inductance stands for the size of the kinetic energy storage, i.e., the effective mass, the capacitance reflects the potential energy storage, i.e., the spring constant and the resistor models the dissipative processes [8]. The parallel capacitance is given by the contacts and cables. The transfer function $Y(\omega)=I(\omega)/U(\omega)$, the so-called admittance is

$$Y(\omega) = \frac{1}{R + \frac{1}{i\omega C} + i\omega L} + i\omega C_0 \quad (1.2.1.1)$$

and is experimentally measurable. Due to the parallel capacitance C_0 there are minimum in the admittance shortly after the maximum. On the resonance the current through the LRC branch flows in the phase with the voltage. The current through the parallel capacitance has a phase shift of 90 degree and causes a small phase shift of the total current. However, the admittance of the capacitance C_0 is small compared to the admittance of LRC branch and can be neglected or compensated electronically with a bridge circuit.

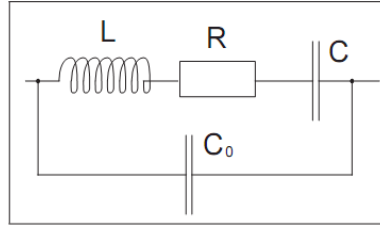


Figure 2. Butterworth-Van Dyke equivalent circuit for a piezoelectric resonator.

1.2.2. Electromechanical coupling

A fit of equation (1.2.1.1) to the experimental data works extremely well. Out of the electrical data the parameters L , R , C and C_0 are obtained. These parameters are not sufficient to determine the mechanical oscillation amplitude. An additional parameter is needed: the piezo-electromechanical coupling constant. It describes the charge separation Q on the electrodes on the piezomaterial per mechanical deflection x : $[\alpha]=C/m$. With a simultaneous measurement of the electrical response and the mechanical amplitude with an optical interferometer this constant can be determined [8]. This constant is characteristic for one type of resonator and a modification, for example the attachment of an object or change of the environment will not alter this constant. The mechanical amplitude can be determined by the current I through the resonator:

$$\begin{aligned} Q &= \alpha x \\ I &= \alpha \dot{x} \\ I_{\text{rms}} &= \alpha \omega x_{\text{rms}} \end{aligned} \quad (1.2.2.1)$$

To model the mechanical resonance, an energetically equivalent mechanical model consisting of one mass and one spring is applied (inset fig 3a). With the knowledge of the electromechanical coupling constant α , the mechanical

parameters can be determined from the electrical parameters by equating the potential energy $Q^2/2C = kx^2/2$ and the kinetic energy $LI^2/2 = mv^2/2$:

$$\begin{aligned} L &= m/\alpha^2 \\ 1/C &= k/\alpha^2 \\ R &= \gamma/\alpha^2 \end{aligned} \quad (1.2.2.2)$$

where k is a spring constant and γ is viscous friction.

From the electrical and mechanical correspondence the voltage can be identified as the driving force: $F = \alpha U$. Figure 4 shows the electric field in the crystal produced by the electrodes and how they are connected. This configuration detects and excites only movements of the prongs against each other. An interesting point to note is that there is a coupling of the two prongs via the piezoelectric effect. When one prong is deflected it produces a charge separation that in turn produces a voltage and thus deflects the other prong in the opposite direction. Assuming the QTF is not connected to any other electronics the charge is converted into a voltage over the capacitance C_0 of the electrodes and the coupling constant is then $\alpha^2/C = 57 \text{ N/m}$. However, if QTF is connected to cables, the capacitance is much larger and the coupling can be neglected. In the case of a fixed voltage (low impedance) the coupling is zero.

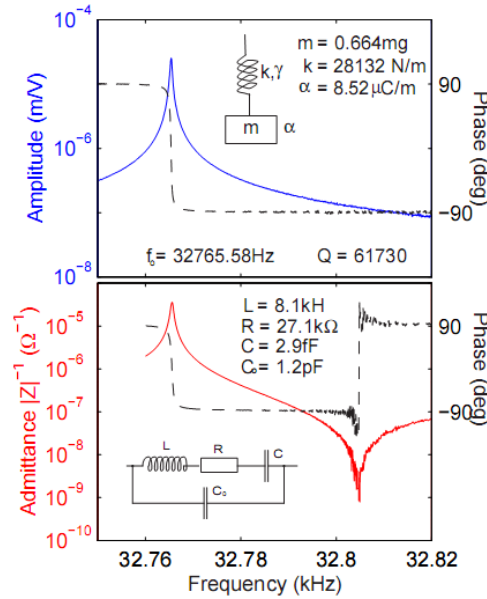


Figure 3. (a) Experimental measurement of the mechanical displacement of the front of a tuning fork prong at room temperature and a pressure of 10^{-6} mbar. The inset shows an energetically equivalent mechanical model (both prongs included). (b) The simultaneous experimental measurement of the electrical response. The inset shows the parameters for the electrical equivalent circuit.

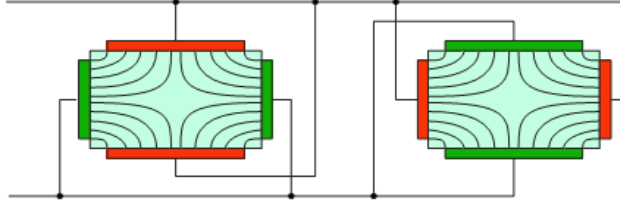


Figure 4. Illustration of the electrical field lines in the cross-section of the QTF. The electric field along the horizontal direction causes a contraction or dilatation of the quartz in the direction perpendicular to the drawing plane. Only the movement of the two prongs in the mirrored fashion is electrically excitable or detectable.

1.2.3. Mechanical model

The mechanical model described in previous section energetically models the proper QTF mode and is appropriate for the determination of the oscillation amplitude. However, questions concerning asymmetries of QTF as they occur when preparing the QTF for the dynamic force detection (see chapter 2), cannot be answered with this model. A model that takes the two prongs into account has to be applied and is shown on the right in figure 5. This system has two modes, symmetric (in-phase) and antisymmetric (anti-phase), that are degenerate for vanishing coupling. The coupling splits the two frequencies and the two modes get mixed when the symmetry is broken. This model, however, cannot explain why the counter oscillating mode has a much higher quality factor than the synchronous mode, and thus is not the appropriate model for QTF. The model on the left in figure 5 has a third mass that models the movement of the base. In this model the counter oscillating mode still has a high quality factor because the center of mass stays at rest and all the forces are compensated inside the fork. The synchronous mode however, produces reaction forces in the support of the base and undergoes much stronger damping. This model also explains the reduction of the quality factor when the symmetry is broken (e.g. by the attachment of additional mass to one of the prongs). Examination of the model with the help of the Laplace transform and the influence of asymmetry is given in [5]. Numerical values obtained using this model are in a good agreement with experimental data. For example in figure 6 the calculated quality factor as a function of the additional mass is shown [5].

In conclusion it can be noted that the symmetry of the tuning fork is very important for a high quality factor. Any asymmetry lets the reaction forces act on the base of the tuning fork causing additional damping. Furthermore, other modes of the QTF do not generally interfere with the proper mode or have a much lower quality factor. This is in contrast to the model of two coupled oscillators, where the degeneracy is only slightly resolved by the coupling and the quality factors of both modes are approximately the same.

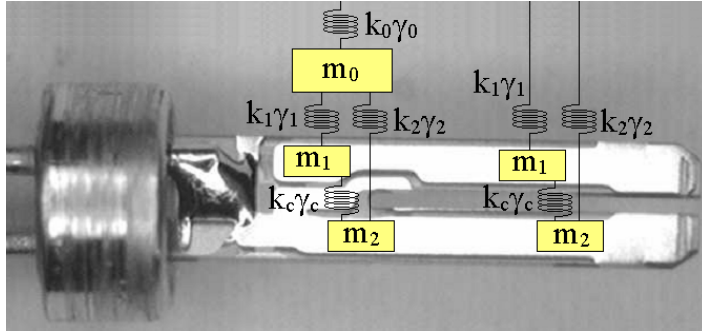


Figure 5: (right) Two coupled oscillators as a mechanical model for the QTF. (left) A model with a third mass to explain the influence of asymmetry on the quality factor.

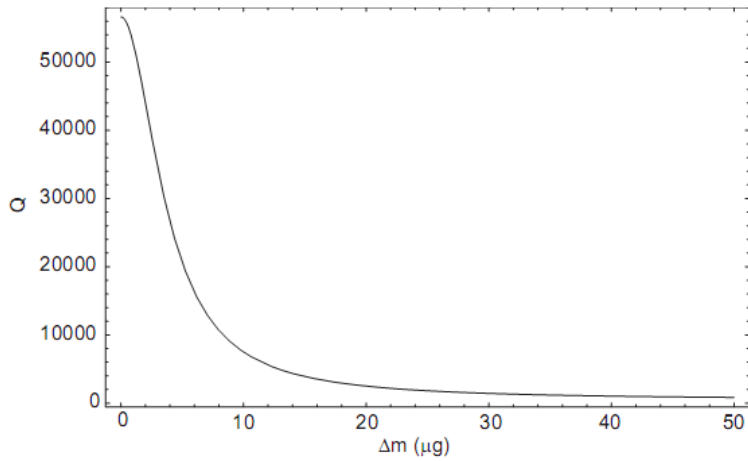


Figure 6: The quality factor is reduced significantly when an additional mass is brought on to one of the prongs.

I.3. QTF as a sensor

Besides the main application as time standard, QTF is also a perfect device for making various sensors [2, 3, 9, 13]. Resonant frequency of the QTF is highly sensitive to some important parameters including added mass, density of surrounding media [9], as well as forces (load) acting on the crystal.

Currently, the most commonly used resonant sensors are plate-shaped quartz crystal microbalances (QCMs) with operation frequency ranging from one to several tens of MHz [10]. QTF is considered to be a cost-effective and simple alternative to QCM, as it has certain advantages. It has more stable resonant frequency. The electronics is simpler due to the considerably lower working

frequency. Moreover, lower frequency is preferable if measurements are made in liquid, since viscosity and other properties of the liquid can cause increased measurement uncertainties under high frequency excitation [11]. Unlike QCMs with thickness shear mode (TSM), QTF employs the flexural mode. Since the vibration amplitude of flexural modes is at least one level bigger than that of TSMs, the QTF is more sensitive to the external perturbations [9].

High sensitivity to mass loading is one of the most important properties of QTF in terms of sensing. The resonant frequency shift due to the mass loading on the QTF beams can be expressed by the simple equation [3]:

$$\Delta f_0 = \frac{f_0}{2m} \Delta m \quad (1.3.1)$$

where m and Δm are the actual mass of QTF beam and the added mass, respectively. It should be noted that the formula is only valid in case of uniform rigid film covering both beams entirely.

The mass loading sensitivity of the tuning can be defined as:

$$S = \frac{\Delta f}{\Delta m} = -\frac{f_0}{2m} \quad (1.3.2)$$

For the 32768 Hz QTF the sensitivity is in order of 10 ng/Hz [3], which is sufficient to sense monomolecular layers of material. This value is ~10 times smaller than for 10MHz QCM. However, for the QTF ~10 times higher counter accuracy can be employed due to lower working frequencies. In total, the sensitivity of QCM and QTF is of the same order of magnitude.

The ability to sense the small mass is used not only for direct mass measurements. The QTF can be coated or modified chemically to achieve the selective sensing. This idea is successfully applied in biosensing [2, 3]. For properly modified QTF frequency shift will take place only in case of specific bonding. It gives the ability to determine the presence of certain substances.

QTF can also be used to sense humidity if coated with appropriate water adsorbing film [12]. Additional mass originating from the adsorbed water will result in resonant frequency shift. The amount of adsorbed water depends on humidity.

Gas [9] and liquid [13] density sensors are another useful applications of QTF. On the basis of equations given by Zhang et al [3] the resonance frequency shift due to the density of the media can be written as:

$$\Delta f_0 = \frac{f_0}{2m} \left(0.6n\rho_L (lt)^{3/2} + 2 \left(\frac{\omega_0 \rho_L \eta_L}{2} \right)^{1/2} \frac{A}{\omega_0} \right) \quad (1.3.3)$$

where $n = 0.2429$ is a constant [4], ρ_L and η_L are density and viscosity of the media respectively, ω_0 is an angular resonance frequency.

In spite of all advantages, there is also a serious drawback that restricts the wide spread of QTF application in biosensing. Most of biological reactions take place in aqueous solutions. Moreover, *in situ* and real-time measurements are often demanded. Water is also most common solvent in chemistry. However, the arrangement of electrodes prevents the use of QTF in media with high dielectrical permeability like e.g. water. Thus, the choice of liquids for QTF measurements is limited to some organic solvents.

On more important application field for QTF is a force sensing. QTF is capable of sensing forces as small as e.g. interatomic interaction between the tip and the surface, and thus can be used as a sensor in Atomic Force Microscopy (AFM) [14]. More detailed description is given in next chapter where main principles of AFM are considered.

I.4 The Phase Locked Loop (PLL)

Since the QTF resonance is at a quite low frequency (33kHz), digital signal processing (DSP) can be applied. This is of great advantage because no analog devices can have a relative accuracy of 10^{-9} or better. As shown in figure 3 the phase between the excitation signal and the current through the fork as a function of the frequency is very steep at the resonance (about 180 degree/Hz). This allows to detect any shifts in the resonance frequency very sensitively. With a controller the excitation frequency is then automatically adjusted to maintain the phase at the value of the resonance. This is the idea of the PLL example of which is schematically shown in figure 7.

The deviation of the phase is detected with a digital two channel lock-in amplifier (SRS 830), which is synchronized by a digital signal from the frequency generator. The lock-in amplifier generates two orthogonal sinus signals as reference for the two channels. The phase of this reference signals with respect to the external synchronization signal can be shifted by an arbitrary value and is adjusted to have the x-reference signal in phase with the signal of QTF at the resonance. Ideally this phase shift would be zero (fig. 3), but the current-to-voltage converters and the long coax cables cause an additional phase shift. The output of the y-channel, which indicates any deviation from the resonance, is fed into controller to control the frequency to the resonance.

For very sensitive force detection parameters can be adjusted to achieve resolutions of the order of 1 μ Hz. However, the stability of the reference frequency is specified to be 100 μ Hz/ $^{\circ}$ C and for the ultimate frequency shift detection an external reference frequency with a temperature controlled quartz oscillator or an atomic clock should be employed.

The oscillation amplitude of QTF is detected with the x-channel of the lock-in amplifier and the output signal is kept constant by a second feedback loop, which controls the amplitude of the excitation signal. This simplifies the interpretation of the different recorded signals, since the mechanical oscillation amplitude of QTF can be assumed to be constant. Second, the transients are

avoided that occur in response to a sudden change in the damping and could last up to seconds for high quality factors.

The PLL provides two signals that indicate the frequency shift and the excitation amplitude. Both signals can be used to control the probe sample distance by the z-feedback controller.

The power dissipated in the tuning fork is the product of the current and the voltage multiplied by the cosine of the phase angle between the two signals. The phase angle is zero on the resonance and is locked by the PLL. The current is kept constant by the amplitude controller and therefore the amplitude of the excitation signal is a direct measure for the power dissipation. Any additional damping caused by probe sample interactions can be detected very sensitively in this manner. Additional power dissipations of the order of 1fW can be detected [5]. This corresponds to an energy loss of 0.2eV per cycle of the tuning fork with typical oscillation energy of the order of 105eV (for 1nm amplitude).

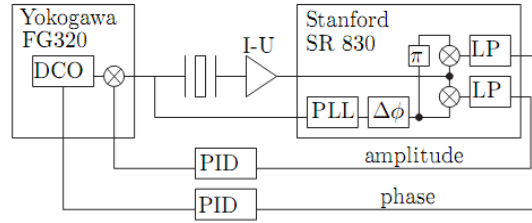


Figure 7: An example of phase locked loop for measuring the frequency shift of QTF.

1.5. Fundamental limits for the force detection with QTF

Fundamental limits for the dynamic force detection with a QTF [15] can be considered applying the formalism introduced by Albrecht [16]. As a mechanical model the simple spring mass model shown on the right in figure 5 will be applied. While absolutely correct for the modeling of the proper QTF mode, the complications arising from having two prongs are avoided. For the parameters given in figure 8, the thermal white noise drive is $192\text{fN}/(\text{Hz})^{1/2}$ at 300 K and $11\text{fN}/(\text{Hz})^{1/2}$ at 1K. Multiplied with the transfer function for the mechanical model, the spectral thermal motion results and is shown in figure 8. Assuming that the deflection detection can detect such small motions, the minimum detectable force gradient [15]

$$F'_{\min} = \sqrt{\frac{4kk_{\text{B}}TB}{\omega_0 Q \langle z_{\text{osc}}^2 \rangle}} \quad (1.5.1)$$

is 4.3mN/m at 300K for a detection band width of 100 Hz and an amplitude of 1 nm. The value gets smaller for low temperature (1K), smaller bandwidth (10 Hz) and larger amplitude (30nm): 3μN/m. However, experimentally this will be hard to realize, since the frequency shift that has to be detected is as low as 3μHz. This corresponds to a relative frequency shift of 10^{-10} , which demands for a stability of the reference frequency that exceeds the values of standard equipment. To reach the thermodynamic limit with QTF, the deflection detection has to be able to detect the thermal noise off the resonance. For a current to voltage converter with a noise of $100\text{fA}/(\text{Hz})^{1/2}$ the thermodynamic limit at room temperature could be reached with a detection band width of about 10 Hz. For the low temperature case, this is not possible with such a current to voltage converter. With a sensitive charge detector with a noise of $001\text{e}/(\text{Hz})^{1/2}$, however, the thermal noise of the QTF at low temperature is dominant over a band width of about 50Hz. In conclusion it can be stated that to reach the thermodynamic limit for force detection, the detection bandwidth has to be narrowed or the quality factor has to be reduced to have the thermal noise of QTF dominant over the deflection detection noise. Experimentally one has to worry also about other sources of noise that could exceed the thermal noise of QTF. For example the noise of the excitation signal has to be smaller then $13\text{nV}/(\text{Hz})^{1/2}$ which produces a force αU that corresponds to the thermal white noise drive of $11\text{fN}/(\text{Hz})^{1/2}$ at low temperature.

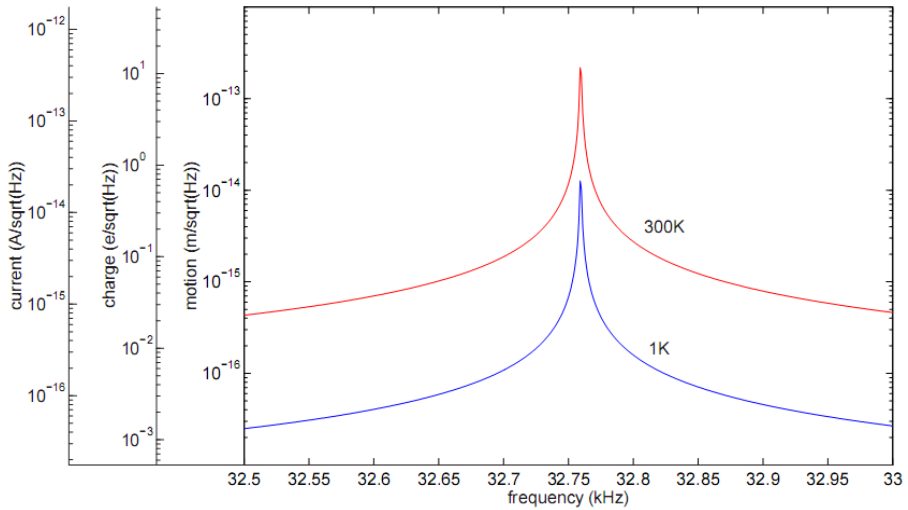


Figure 8. The thermal motion of QTF at room temperature (300K) and at 1K. The motion is converted into a charge via the piezo-electro-mechanical coupling constant and into a current by multiplying the charge with the frequency.

It can be concluded that QTF is a powerful device for making various sensors having number of advantages over alternative devices including high q-factor, frequency stability, low cost, and elaborated models.

2. ATOMIC FORCE MICROSCOPY – GENERAL DESCRIPTION AND TIP CONTAMINATION PROBLEM

Atomic Force Microscopy (AFM) belongs to scanning probe microscopy (SPM) – the powerful morphological and structural analysis technique based on the sharp probe scanned over the sample surface, which has been employed in the analysis of a large range of materials with atomic resolution [17]. Application of AFM for manipulation of nanostructures and measurements of frictional and mechanical properties will be considered in the next chapter. The use of AFM tip in creation of QTF-based force sensor and appropriate AFM tip cleaning technique will be treated in results section. Here, a general description of AFM and QTF based AFM, tip contamination problem, and existing tip cleaning techniques are reviewed.

Since AFM is widely used in various research fields and its detailed description can be found elsewhere [18], only the basic concepts are described.

2.1. Atomic Force Microscopy

The principle of AFM relies on the use of a sharp tip mounted on a cantilever which is brought into close proximity to the surface where intermolecular forces acting between the tip and the surface cause the cantilever to bend (Figure 9). The tip is scanned over the surface and images are obtained by recording the cantilever deflections during scanning detected with laser beam focused on the top of the cantilever.

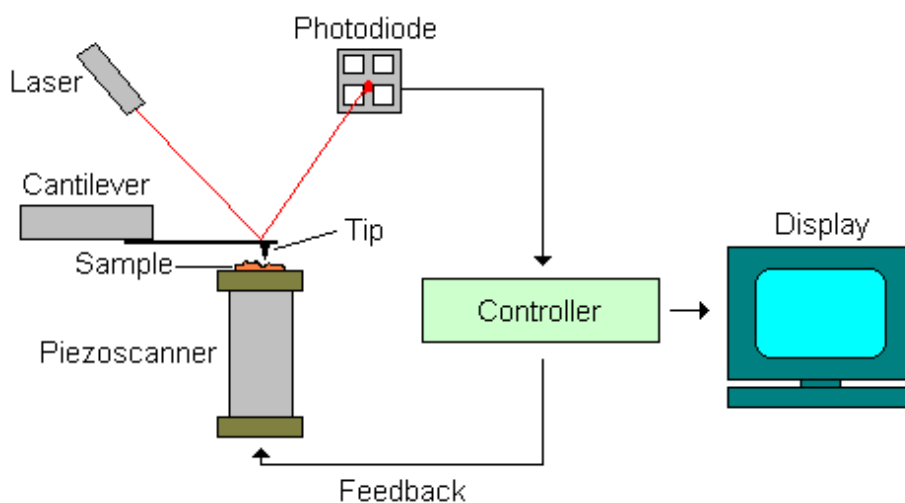


Figure 9. AFM operation principle.

There are several operating mode in AFM technique. The general modes are *contact mode*, *non-contact mode* and *dynamic contact mode* (also called *intermittent contact* or *tapping mode* as patented by Bruker). In non-contact mode the attractive forces (generally the Van der Waals forces) are used to hold the tip above the surface. This prevents sample from harming. In contact mode the repulsive forces tend to dominate. The measurable forces in AFM technique are between 10^{-9} - 10^{-8} N. The figure 10 illustrates dependence of the force (F) between the tip and the sample on distance (R) between them.

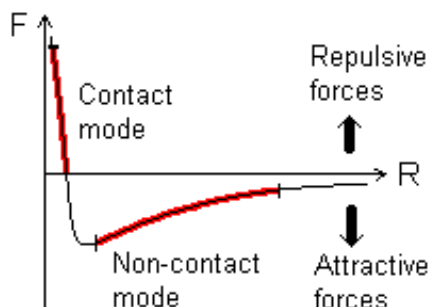


Figure 10. dependence of the force (F) between the tip and the sample on distance (R) between them.

Tapping mode is the most commonly used of all AFM modes. Tapping mode imaging is implemented by oscillating the cantilever assembly at or near the cantilever's resonant frequency using a piezoelectric crystal. The piezo motion causes the cantilever to oscillate with a high amplitude (typically greater than 20nm) when the tip is not in contact with the surface. The oscillating tip is then moved toward the surface until it begins to lightly touch, or tap the surface. During scanning, the vertically oscillating tip alternately contacts the surface and lifts off, generally at a frequency of 50,000 to 500,000 cycles per second. As the oscillating cantilever begins to intermittently contact the surface, the cantilever oscillation is reduced due to energy loss caused by the tip contacting the surface. The reduction in oscillation amplitude or frequency is used to identify and measure surface features. Also, the phase shift between the input and output to the cantilever can be detected.

Tapping mode overcomes problems associated with friction, adhesion, electrostatic forces, and other difficulties that plague conventional AFM scanning methods by alternately placing the tip in contact with the surface to provide high resolution and then lifting the tip off the surface to avoid dragging the tip across the surface. When the tip contacts the surface, the high frequency makes the surfaces stiff (viscoelastic), and the tip-sample adhesion forces is greatly reduced. Tapping mode inherently prevents the tip from sticking to the surface and causing damage during scanning. Unlike contact and non-contact

modes, when the tip contacts the surface, it has sufficient oscillation amplitude to overcome the tip-sample adhesion forces. Also, the surface material is not pulled sideways by shear forces since the applied force is always vertical. [19]

The use of modified probes enable much more specific information, such as frictional, magnetic, and thermal properties of the surface being investigated. Different areas of a sample can cause different cantilever twisting depending on frictional forces acting between the tip and the surface. [20]

2.2. QTF in AFM

QTFs were introduced into SPM by Gunther, Fischer and Dransfeld [21] for use in scanning near field acoustic microscopy and later by Karrai and Grober [22] and others [23], as a distance control for a scanning near field optical microscope (SNOM). In these microscopes the optical fiber tip is oscillating parallel to the surface resulting in shear force detection. Shear forces were then explicitly investigated using QTFs by Karrai and Tiemann [24]. QTFs with a magnetic tip were also used for magnetic force microscopy [25]. Rensen et al. were able to resolve atomic steps with an atomic force microscope (AFM) [14] cantilever and Si-tip attached to the QTF [26]. Giessibl et al. demonstrated atomic resolution on the Si (111)-(7x7) surface using QTF with one prong fixed (qPlus Sensor) [27]. Since only two electrical contacts are necessary for the operation, QTFs are simple to integrate in SPM even in a cryogenic environment. The application of the QTFs for scanning probe microscopy at low temperatures was demonstrated by Rychen et al. [28]. Rozhok et al. [29] improved the construction of the sensor proposed in Rensen et al. [26] by gluing only the tip from AFM cantilever to one prong of QTF.

Main Advantage of QTF-based AFM over the conventional AFM are simple feedback electronics, compact design, and absence of optical detectors, making it well suited for use at cryogenic temperatures or inside electron microscopes for enhanced features like real-time observation of tip-substrate interaction etc.

Compared to micromachined AFM Si cantilevers the QTFs are very stiff. The problems concerning the nonlinearity of the oscillator motion in the interaction potential are reduced due to the high spring constant compared to the interaction forces. The stiffness avoids the snap in to contact and thus allows operating it with lower amplitudes than a cantilever. This simplifies the interpretation of the signals when the short-range interactions are investigated. The high stiffness is also of advantage for nanomanipulation applications as for example nano-lithography and manipulation. However, it is a disadvantage for the detection of very small forces, and is a danger for the tip to be crashed since the force is not limited by a soft spring.

QTFs are insensitive to high magnetic fields and operate well at low temperatures. The fact that no light is needed for the deflection detection is important for the investigation of semiconductor heterostructures, which show the

persistent photo effect. Any light scattered on to the sample would alter its properties permanently.

Due to the high q -factor, dynamic force microscopy even in liquids is possible. The perspective to use them as a carrier for sensorslike field-effect transistors (FETs), single-electron transistors (SETs), superconducting quantum interference device (SQUIDs) and hall sensors makes them attractive especially for the investigation of super- and semiconducting nanostructures in combination with transport experiments.

The direct electromechanical coupling also allows to calculate the dissipation power, widely used in tribological measurements, easily and accurately without the troubles of calibration ($U \times I \times \cos(\theta)$). This is a very powerful advantage of piezo electric oscillators in dynamic force microscopy. [5]

2.3. AFM tips and tip contamination

The most common tip material in AFM techniques is silicon nitride (Si_3N_4). This material is very hard which is necessary when the tip is dragged over the sample. It has outstanding wear resistance and good chemical resistance. Also, single crystal silicon can be used. It is somewhat less resistant to wear, but the tip can be made sharper, less than 10 nm as compared to 20–60 nm for silicon nitride. [30] Typical AFM cantilever with the tip is shown in figure 11.

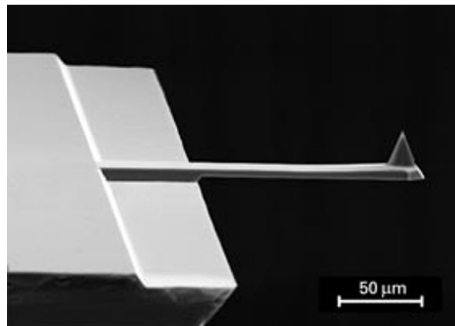


Figure 11. Typical AFM cantilever with the tip (MikroMasch)

Ideally tip apex must be round shaped and terminate with the single atom. However, scanning process or even exposure of AFM tip to ambient conditions can lead to morphological changes in physical profile of the tip and cause deviations from ideal shape and result in artifacts in the scanned image. There are a number of tip defects, which cause artifacts. The most common are:

- a) Multiple peaks on the apex being atomic scale protrusions. Every peak during scanning contributes in the tip-sample interaction. In the simplest case of double peak apex the features on the sample surface look twin in the

- scans. Absence of this defect is especially crucial when measuring single macromolecules.
- b) Flattered apex. This results in lowering of resolution power. The sharpness of the apex tends to decrease during consecutive contact mode scans of the sample surface.
 - c) Non-spheric apex. Results in geometry distortion of sample features.

These changes are caused by two main mechanisms: material aggregation on the tip, and breakage, or wear, of some regions of the tip. The first mechanism, material aggregation, is the most frequent and can be regarded as an unavoidable consequence of the scanning process in certain cases [31, 32]. The aggregated material, organic or inorganic, comes from the sample itself, or a contamination layer, always present on the surface of a sample exposed to ambient conditions. Even if great care is taken during the scanning process, loose particles may attach to the tip during its contact with the sample surface. Consequently, tip effective dimensions are altered (enlarged), decreasing the image spatial resolution. Generally, material aggregation is the main cause of tip deterioration during investigations of soft samples (e.g. polymers and biological materials) and also brittle samples (e.g., oxides;) [31, 32]. Tips can be contaminated during the fabrication process or storage as well. Thus, even the new tip may require cleaning to increase the image resolution.

2.4. Common Tip Cleaning Methods

The general difficulty, concerned with cleaning of the SPM tip, is its small dimensions. The most of usual cleaning techniques will certainly destroy the tip. In the present day several different physical and chemical methods are used to remove contaminations from the tip surface. The most frequently used are UV-ozone treatment [33-35], various wet processes, [36, 37], plasma etching [38], as well as all possible combination of existing methods [39].

2.4.1. UV-ozone treatment

UV-ozone treatment is the most common and is very efficient in removal of various hydrocarbons. As a pretreatment the tip placed in oxygen at atmospheric pressure and irradiated by UV-light of 185 and 254 nm. In these conditions, oxygen is excited to be ozone or radical so that some hydrocarbons are decomposed under UV irradiation by forming volatile molecules such as H₂O and CO₂. Then, the clean silicon surface is obtained by growing a thin oxidized layer on the tip surface by heating it in oxygen at low pressure with subsequent removal of this layer by annealing in ultra-high vacuum (UHV) condition [33] or by reducing it in suitable acid solution [34]. Heating at high temperatures and for a long time to remove the oxide layer possibly makes the tip blunt, because formation of volatile molecule as SiO on a SiO₂ surface needs a Si atoms supplied from the inside, causing corrosion of the Si tip.

2.4.2. Wet processes

There are lot of acid solutions were tested and some of them with certain limitations were successfully employed as a cleaning agents for SPM tip (so-called acid bathing). Among them are sulphuric acid, hydrochloric acid (HCl), hydrofluoric acid (HF), and sulfochromic acid solutions under a range of concentrations. HF solution is the most common. It is very efficient in removing large amounts of inorganic material, and, therefore, is considered an excellent cleaning option when only inorganic contamination is present. But it must be noted that HF solution is very aggressive to the tip and eventually damages it if long bathing times are employed. Besides cleaning effect HF treatment can make the tip sharper [33].

The cleaning efficiency of the HF solution for different types of inorganic contaminants may not be associated with a direct attack on the aggregated material. Rather it seems to be associated with the removal of the silicon oxide layer that always covers a silicon-made SPM tip, either new or used. It is well known in the semiconductor community that HF readily dissolves silicon oxide [40]. Removing an oxide layer, where the inorganic contaminants are attached, leads to cleaning of the SPM tip. This oxide removal may also explain the sharpening effect. However, such a general and, apparently, contaminant-independent mechanism is not very efficient when only organic material is aggregated to the tip. A possible explanation for this may arise from shielding effects of a compact organic layer covering the tip. While it is expected that hard inorganic materials cover the tip unevenly, forming holes where the cleaning solution can penetrate and dissolve the underneath silicon oxide layer, it is supposed that soft organic material may cover the tip evenly, producing a shield without holes, which precludes the penetration of the HF solution and, therefore, the organic contamination removal.

In contrast with HF solution, the cleaning efficiency of HCl solutions is not related to silicon oxide dissolution, as it is insoluble in HCl [40]. Hence, it might rather be associated with a direct attack on the inorganic contaminating agent.

Despite the fact that cleaning with acids is fast and easy, other cleaning procedures are often preferred because of avoiding chemical damages to other parts of the cantilever including a piezoresistive film and a Si tip.

Less aggressive wet cleaning processes are based on the solvents like toluene [41], ultrapure acetone, tetrahydrofuran, ethyl alcohol, isopropyl alcohol, deionized water etc. Ultrasound can be noticeably helpful in the wet cleaning processes. With its help, even water (bi-distilled and de-ionized) can be used for tip cleaning [42]. Due to its strongly damaging action on many adhesive joints, water is a suitable liquid for cleaning by ultrasonic cavitation, dispensing with the use of any other cleansing agent, and it is recommended for the removal of particles in the micrometer size range, from solid surfaces. The fast periodic compression and decompression of high-surface tension liquid such as water produces a myriad of micro bubbles bursting within the liquid, especially at the existing solid-liquid surfaces. The resulting pressure gradients are sufficient to dislodge the particles, but they can also produce geometrical deformations at the surfaces [43]. The

cleaning time should be kept as short as possible, to avoid probe break-down. In some cases, the adherent particles could not be removed in a single step and cleaning procedure has to be repeated to achieve satisfactory results.

In the electronics industry to clean silicon and silicon nitride surfaces so-called piranha solution is used. It consists of sulphuric acid and hydrogen peroxide mixture. Dipping the tip in a piranha solution for 30 minutes can remove silicon oil contamination often introduced from the cantilever packing material [43].

2.4.3. Plasma Etching

Plasma etching, derived from the electronics industry, is known to remove organic contaminants from silicon and silicon nitride surfaces [43]. Usually hydrogen, oxygen or argon plasma is used. It reacts with carbon compounds or oxides on the tip surface.

2.4.4 Combined Methods

Sometimes it is reasonable to use different combinations of the existing cleaning methods. In this area, one of the most efficient combinations for organic removal involves UV/ozone exposure followed by ultrasonic solvent baths (15 min. in acetone and 30 sec. in isopropyl alcohol) [39]. The role of both solvents is only to help remove the fragments of organic material which were modified (chemical bonds broken), oxidized, and even vaporized by the long exposure to the ultraviolet radiation and ozone combination.

The combination of the sulfochromic solution with UV/ozone exposure and HCl acid solution bath can give satisfactory results in many cases [39]. Sulfochromic solutions constitute a well-known type of glassware cleaning agent. They are regarded as very efficient in removing organic and inorganic contaminants without damaging the glass surface. The most efficient sulfochromic solution had the following composition: 20% (v/v) of concentrated sulphuric acid, 17% (v/v) of potassium dichromate, and 63% (v/v) of demineralized water. Furthermore, it was observed that the efficiency of the sulfochromic solution increases as the temperature increases and, thus, it should preferably be used at boiling temperatures.

In comparison with the specific cleaning processes, the combined methods are not as fast and not as simple. Therefore, it can be suggested that if there is only one type of tip contamination and its nature is known, it may be faster and simpler to employ the specific methods. On the other hand, if it is known that there are both organic and inorganic contaminants, or the nature of contaminations is ignored, then it is more effective to employ the generic method.

The effectiveness of each method depends on the nature and amount of the tip contamination. There is also a serious risk of impairing the tip. Thus, the employment of a given cleaning procedure may or may not result in effective contaminant removal. Moreover, the existing cleaning methods require the tip to be taken out or at least moved from its position above the sample.

3. NANOTRIBOLOGY AND MANIPULATION OF NANOSTRUCTURES

3.1. Nanotribology

Recent endeavors to understand nanometer scale friction, adhesion, and wear, as well as the related possibilities to control them, have generated an interdisciplinary scientific area – nanotribology, addressing pure and applied cutting-edge research topics with tremendous potential impact on technology and everyday life, including safety, economy, life quality, energy and material saving, towards a sustainable development.

The science underlying friction is a very long-standing problem. After centuries of scientific and technical development, friction and the related phenomena constitute a vast and interdisciplinary field. Understanding the complex processes occurring at the interface of two materials in relative sliding motion (the science of tribology) is central to pure and applied sciences, e.g. in studying plastic deformation and fracture development in a contact zone, as well as to many technological problems including lubrication, wear, fatigue etc. Especially at the smaller microscopic scales, interfacial forces become dominant due to the increase in surface-to-volume ratio. In nanotechnology, for example, friction and adhesion are limiting factors that constrain performance and lifetime of microdevices, such as magnetic storage systems, micro-/nano-electro-mechanical devices (MEMS/NEMS), and aerospace components. Durable low-friction surfaces, wear-resistant materials and coatings, as well as suitable liquid and solid lubricants are in demand for hi-tech applications.

Recent developments in experimental techniques, dominated by the atomic/friction force microscopes (AFM/FFM), provided insight into the nature of interaction between materials in contact and relative motion at the micro and nanoscale. Based on these atomistic approaches many of the previous primary and historic questions about friction are being reconsidered and freshly answered, and more are emerging. Studies at molecular scales reveal frictional behaviors that are markedly different from those observed in macroscopic systems – empirical laws of friction no longer hold at the nanoscale. The nature of the elementary nanotribological mechanisms, which intimately relate friction, adhesion and wear, and even more the possibility to control them by external means is still in its infancy, and remains a formidable challenge. [44]

3.2. Nanomanipulation

Nanoscale manipulation experiments have two general purposes. On one side they enable investigation of the material frictional, mechanical and other properties at nanoscale. E.g. one of the most fundamental and still unsolved problems in nanotribology (the science of friction at nanoscale) is dependence of friction on real contact area. Its understanding is crucial for filling the gap between nanoscale and microscale friction. From the other side manipulation

experiments have practical aspect. Exact 2D positioning and assembly of nanostructures is essential for nanotechnological applications [45], like e.g. creation of nanoelectromechanical systems (NEMS), for applications in nanoelectronics, in digital information storage etc.

3.2.1. Manipulation of Nanoparticles

The most commonly used tool for the manipulation of nanostructures in general and nanoparticles in particular is the AFM, discussed in more details in chapter 2. Several different approaches have been applied in AFM manipulation strategies. In dynamic mode, particles can be moved during the scanning process when amplitude of the tip oscillations is increased above a certain threshold value. Estimation of frictional force is usually made on the basis of dissipated energy that is calculated from the phase shift as follows [46]:

$$P_{\text{tip}} = \frac{1}{2} \frac{k\omega_0}{Q_{\text{cant}}} (Q_{\text{cant}} A_d A \sin \varphi - A^2) \quad (3.2.1.1)$$

Increasing the scan rate above a certain value rather than increasing oscillation amplitude yields similar results [47]. Another approach consists in switching the feedback off during manipulation [48]. In this case, the tip pushes particles and oscillations are not essential for the manipulation process; cantilever deflection is recorded.

Particles can also be moved in contact mode. For example, Dietzel et al. [49] introduced a so-called “tip-on-top” strategy. In this method, the tip is first positioned on top of the nanoparticle approximately at its center. The nanoparticle then follows the tip motion. The measured torsional signal is directly proportional to the interfacial friction between the particle and the substrate.

AFM manipulations have certain limitations. First, there is no real-time visual feedback concerning the contact geometry or the particle position and behavior during manipulation (i.e., whether it is rolling or sliding). Only indirect conclusions can be drawn based on the shape of the force curves [50]. Additionally, many AFM experiments are made in ambient conditions, meaning that a considerable amount of water is present on all surfaces under investigation, complicating the interpretation of forces.

Another problem is the “aging” of a sample exposed to ambient conditions, resulting in sticking of the particles to the substrate [51]. Sticking increases significantly with time. Given that AFM manipulation experiments are time consuming, adhesion can increase even within single experimental series.

To overcome these obstacles, manipulation experiments should be performed in a vacuum environment with real-time visual control.

3.2.2. Manipulation of Nanowires

Nanowires (NWs) – ultrafine wires having typical diameter in the range of 1-100 nm and high aspect ratio [52]. Tribological studies of NWs are of high relevance from both scientific and technological point of view: NWs are now among most important objects in modern science and have number of promising applications in nanotechnology. Mechanical and electrical properties of NWs may be superior in comparison to corresponding bulk material [53]. NWs can be made from a wide range of materials, and can be metallic, semiconducting or insulating. Semiconductor nanowires made of silicon, gallium nitride and indium phosphide have demonstrated remarkable optical, electronic and magnetic characteristics (e.g., silica nanowires can guide light around very tight corners) [54]. NWs have potential applications in high-density data storage, either as magnetic read heads or as patterned storage media, and electronic and optoelectronic nanodevices, for metallic interconnects of quantum devices and NEMS [55]. Plenty of prototype devices based on NW were already demonstrated during last few decades including sensors, resonance-tunneling diodes, light emitting diodes, photodetectors, electromechanical devices, piezoresistors and etc. [56-62].

Zinc oxide (ZnO) is one of the materials commonly used in NWs preparation. ZnO NWs have some interesting properties, like e.g. electric-field mediated tunable photoluminescence with potential applications as novel sources of near-ultraviolet radiation [63]. ZnO NW can also be used to produce a p-n junction that serves as a diode [64]. ZnO NW gas sensors are also reported [65].

Considering that fabrication of NW-based devices requires precise control over positioning and subsequent behavior of the NWs, it is evident, that deeper understanding of NW-surface bilateral tribology mechanisms is crucial from applicative point of view.

Number of methods of investigation of mechanical properties of NWs or nanotubes (NT) have been developed. Ambient AFM can be used for vertical loading of a nanowire suspended over a hole or a trench to determine Young modulus and mechanical strength. This method was applied on Ge NWs and carbon NTs (CNT) [66, 67]. Elastic properties and mechanical strength of SiC NWs and CNT deposited on low friction substrate (MoS_2) and pinned from one end by evaporated metal pads were measured using AFM lateral force regime [68].

Common method of NW's Young modulus determination consists in finding the resonance frequency of a NW fixed from one end and placed inside scanning electron microscope (SEM) by sweeping the frequency of external excitation [69]. Another method is based on lateral bending of NW free end by pushing it with calibrated contact mode AFM cantilever, while NW second end is fixed on an edge of rigid substrate. Elastic deformation force is calculated from visual deformation of a NW and a calibrated AFM cantilever inside SEM. Method was applied to investigate ZnO NWs [70]. Axial loading or stretching of NW glued between rigid substrate and calibrated AFM cantilever or between

two AFM cantilevers was applied for Si and B NWs, as well as CNTs Si, B NW and CNT [71-74]. Analogous axial tensile in situ tests performed on ZnO and Si NWs using MEMS-based nanoscale material testing stage inside transmission electron microscope (TEM) [75, 76]. Real-time force measurement during NW bending was performed by contact mode AFM inside SEM to measure Young modulus of vertically grown arrays of SnO₂ NWs [77].

Only few works reported of measurements of kinetic friction of NW on flat substrate. Manoharan et al. examined the kinetic friction force during dragging of a ZnO NW parallel to its axis at different loading forces measured by MEMS force sensor at ambient conditions [78]. Conache et al. reported distributed static and kinetic friction of InAs NWs on Si₃N₄ coated Si wafer based on measuring curvature of ultimate NW bending radius after AFM manipulation at ambient conditions, where friction was calculated using Young modulus of a bulk material for calculations [79]. In other words, existing experimental methods and theoretical models for measuring and description of tribological properties of NWs contain significant uncertainties and do not include all important parameters. Thus, it can be concluded, that NW research is in preparatory phase and its potential is not realized.

4. STRUCTURAL PROPERTIES OF NANOPARTICLES

Nanoparticles (NPs) are often considered as a fifth state of matter. They have some properties, unlike either the molecules or the bulk and in that sense represent a transition between those states. Many effects can appear in nanoparticles, which are not observed in the bulk crystals. One of the most common NP material used in nanoscience and nanotechnology in general and in nanomanipulation experiments in particular, is gold (Au). Au NPs were thorough investigated both theoretically and experimentally in present thesis. This section provides necessary background of some particular properties of NPs in general and Au NPs in particular, like shape and surface energy, which are essential in the context of nanomechanics, nanotribology and nanomanipulation. Gold belongs to elements with face centered cubic lattice (fcc) and its structural properties can be considered in terms of fcc materials in general.

4.1. Structural Properties

Important property of NPs is that their shape and crystal structure differs from that of the bulk material. The main reason is the nature of the forces such as surface tension, acting on NP [80]. The most frequently observed shapes at the nanometric scale are shown in Fig. 12. They correspond to the cuboctahedron, the icosahedron, the regular Bagley decahedron, the star particle, the Marks truncated decahedron, and the round pentagonal configuration. The latter shape has several variants such as the truncated octahedron or the tetrakaidecahedron. The regular decahedron, the star, the round pentagonal, and the Marks decahedron are variants of the decahedron shape and correspond to one of the most important shapes because they are very stable and frequently observed.

Particles of fcc materials have many variants of the basic shape and correspond to different truncations of the cuboctahedron. The most commonly observed are the truncated octahedron and the tetrakaidecahedron. For the case of gold and silver, all the forms of the truncated decahedron and the icosahedron become the most favorable shape. Another variant of fcc particles is the tetrahedral particle, which in a truncated version becomes flat platelets.

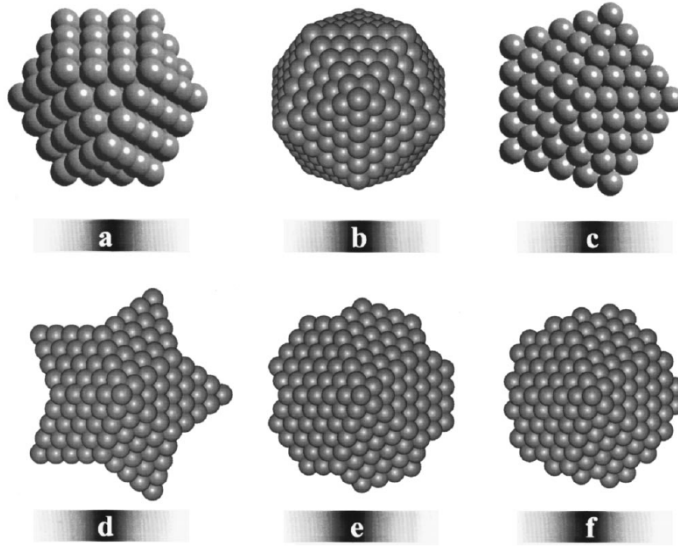


Figure 12. Main types of particles which are observed at the nanometric scale corresponding to (a) fcc cuboctahedron, (b) icosahedron, (c) regular decahedron, (d) star decahedron, (e) Marks decahedron, and (f) round decahedron.

Faceting and truncation are the most favorable mechanisms chosen by nature for minimizing the total energy of the particle. This is valid even for the fcc shapes in which a pure cubic particle has never been observed. The formation of extra facets induces the reduction in the contributions to the energy coming from the surface area and from the radius of curvature of the particles. As discussed by Cleveland et al [81] and Patil et al. [82] using macroscopic concepts as a guide, a particle at 0 K should have a total energy (E_t) given by

$$E_t(N) = E_B N + E_\sigma + E_\gamma, \quad (4.2.1)$$

where N is the number of atoms, E_B is the bulk energy per atom, E_σ is the strain energy per atom, E_γ is the average surface energy per unit area, and S is the surface area of the cluster. Faceting introduces a minimization of the second and third terms of Eq 4.2.1. Therefore, particles will tend to shapes containing extra facets and to an overall more rounded shape. However, from the point of view of atomistic simulation, the situation is more complex. As the size increases, the internal stress becomes very important, causes some particles such as the icosahedron to increase its energy very rapidly, and becomes less stable despite having the most rounded shape.

As the particles grow larger, they start to produce more internal stresses. This can be considered as a slow transition to the bulk state. Therefore, a stress release mechanism should dominate at a given size. This produces more

complicated structures with various defects. This problem, for the case of decahedral particles, has been discussed theoretically in an extensive way by Gryaznov et al. [83, 84] Those authors suggested several mechanisms for stress release. From their calculations using classical theory of elasticity they conclude that three most energetically favorable mechanisms for stress release are: dislocation formation, formation of a system of thin twin parallel layers in one of the sections of the decahedron, splitting of the pentagonal axis in two or more partial disclinations, and displacement of the pentagonal axis to the periphery of the particle. In general, several release mechanisms are acting at the same time and nanoparticles of a size >10 nm have a complex structure.

It is also important to know the value of the total energy versus the size and structure of the nanoparticles. Some simulations were performed using Lennard-Jones interactions [85] or more sophisticated potentials such as the Finnis-Sinclair and combined Lennard-Jones potentials and three body potentials. [86] The most comprehensive are the ones of Landman et al. [81, 87] Contrary to earlier calculations that consider the icosahedron the most stable structure, Landman's group concluded that one of the most stable structures in some sizes corresponds to the Marks decahedron. However, these calculations consider a relatively small number of atoms.

Yacaman et al [88] have calculated the energy of different structures as a function of the size for wide range of sizes and found that the most stable structures correspond to the truncated decahedral structures: the star, the rounded pentagonal, and the Marks decahedron. Although, for a small number of atoms, the icosahedrons and the regular decahedron are also more stable than the fcc structures. However, when the number of atoms increases, the truncated decahedral structures remain stable over the fcc whereas the icosahedron and the regular decahedron become less favorable. It should be noted that energies are so close that in a given sample it is expected that a statistical distribution of shapes will be observed specially for the case of smaller sizes. In addition, rapid growth conditions in which the particles tend to be out of equilibrium will lead to a more diverse distribution of particles. This is the case for vapor deposition growth. For colloidal methods, which produces slower growth and allows the particles to reach an equilibrium configuration the truncated decahedral shapes should be the predominant structure. This latter fact is confirmed by experimental observations. This is also true for postdeposition annealed particles. [88]

An important case to consider is when the particles are passivated with an organic molecule. In that case, an extra term in the energy is introduced by the interaction between the atoms of the NP and the atoms of the organic molecule. This results in an even higher tendency to produce faceting shapes such as all the forms of the truncated decahedron or the most truncated fcc shapes as shown experimentally by Gutie'rrrez-Wing et al. [89]

The situation with the particle shape is complicated even more by the fact that at nanoscale the shape is not necessarily constant. This is because the energy of a nanoparticle shows many local minima configurations, corresponding to different structures. A small excitation (e.g. by the beam of an

electron microscope) may be sufficient to induce shape transitions on the particle like was shown e.g. by Ijima and Ichihashi [90] for a gold particle of ~ 2 nm size fluctuating between the cubo-octahedral, icosahedral, and single twined structure. In order to explain the structural fluctuations two main models have been proposed. The first one involves the complete melting of the particle followed by a recrystallization to a new structure [91]. The energy for the melting is provided by the inelastic scattering of the incoming electrons on the particle. The second model [92] assumes that different particle configurations have similar energies and the low energy barrier between different configurations allows transition without melting. This phenomenon has been termed quasimelting by Marks and co-workers [92] and refers to the fluid-like behavior observed in the NPs. In some cases, the particle has a transition with a memory of the original crystalline orientation [93]. The latter case involves the appearance, movement, or disappearance of twin boundaries.

Variations in shape and the presence of defects have strong influence on mechanical and tribological properties. In particular, the issue of understanding how friction operates at the nanoscale level is one of the most important issues in nanotechnology. This subject is still an open question and the phenomenon is very complex and requires extensive additional research.

5. AIMS OF THE STUDY

The ultimate goal of the study is contribution to detailed understanding of the interaction mechanisms and properties of materials at nanoscale, and finding critical parameters controlling them. To achieve this goal a number of objectives were assigned, which include both experimental and theoretical aspects. All objectives are interconnected and reinforce each other. The main objectives are listed below.

- Elaboration of the nanomanipulation technique inside a SEM chamber, for real-time measurements of the frictional and mechanical properties of nanostructures (nanoparticles and nanowires).
- Finding relations between morphology and frictional properties for gold nanoparticles manipulated on oxidized silica substrate inside SEM.
- Development of the theoretical model of stress relaxation in gold nanoparticles and nanorods based on the formation of shell layer with crystal layer mismatch.

6. RESULTS AND DISCUSSION

6.1 Applications of QTF in mass, biological and chemical sensing (paper V and patent VII)

In this section the mass sensitivity of QTF is used to elaborate the chemical and biological sensing method for measurements in water, which is impossible with the existing QTF sensors for the reasons described in chapter 1. In all experiments described in chapter 6.1, QTF was driven electrically by AGILENT 33120A Function/Arbitrary Waveform Generator. The frequency response was tracked with a METRIX 3354 oscilloscope. METRIX software was used to record and analyze the data on a PC.

6.1.1. Controlled silanization in vapor

Before development of the QTF sensor for measurements in water, we performed simple experiments with unmodified bare QTF in gaseous atmosphere to investigate its sensing capabilities and test our equipment. Silanization of QTF in gaseous phase was tracked.

QTF, connected to electronic circuit, was placed in hermetically closed vessel and the resonance frequency of QTF was recorded. Then the drop of tetramethoxysilane was placed at the bottom of the vessel and the frequency response of QTF was continuously recorded. During 100 minutes the total resonance frequency shift was 27 Hz (fig. 13). According to eq. 1.1.2.1 it corresponds to 270 ng of added mass. To ensure that silanization and not just condensation of silane took place, the QTF was rinsed in acetone and frequency response was measured again. No restoration of resonance frequency was observed, indicating that silanization was complete.

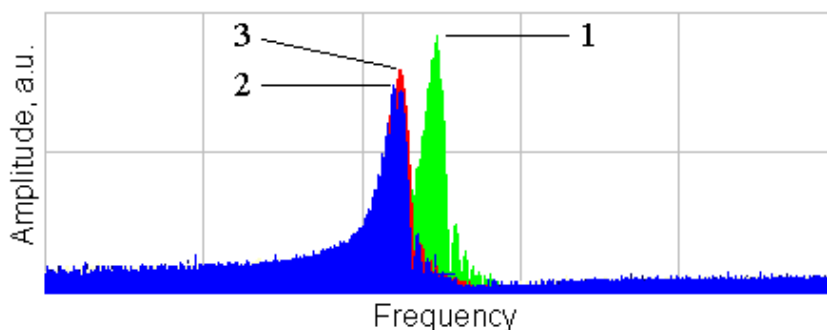


Figure 13. Frequency spectra of vapor phase silanization of QTF. Frequency response corresponds to: 1 – clean QTF in air, 2 – QTF after 100 minutes in silane vapor atmosphere, 3 – QTF after rinsing in acetone and drying. Resonant frequency shift between 1 and 3 is approximately 27 Hz.

6.1.2. Insulation of QTF electrodes

We have tried to insulate the QTF electrodes to perform the measurements directly in buffer solutions, as was suggested by Su et al. [2]. We have tested different coating methods, including silanization, TiO₂ atomic layer deposition, sol-gel and polymer coatings. However, due to the arrangement of the QTF's electrodes, it acts as a capacitor, meaning that if the surrounding medium has a high dielectric permeability, there will be unavoidable capacitive losses, regardless of the presence of the coating.

6.1.3. Integrated carbon nanotube fiber-quartz tuning fork biosensor

In this section, a novel label-free biosensor for in-situ measurements in aqueous solutions is described. The sensor is comprised of a carbon nanotube (CNT) fiber attached to one prong of a QTF. The CNT-fiber was chosen because of its porous structure, low density and high stiffness [94]. Moreover, CNTs can be easily functionalized [95], which is necessary for designing specific bio-recognition assays. The performance of the sensor was demonstrated experimentally by monitoring the adsorption rate of bovine serum albumin (BSA) to the CNT-fiber at two different pH values. According to Valenti et al., BSA is adsorbed directly onto CNTs, with the adsorption rate depending on pH [96]. For the BSA adsorption experiments, pH values corresponding to maximal (pH 4.8) and minimal (pH 7) adsorption rates were selected.

BSA was purchased from PAA Laboratories GmbH. BSA solutions (0.1 mg mL⁻¹, pH 4.8 and pH 7) were prepared in phosphate buffers. Multiwall carbon nanotubes (O.D.×I.D.×L = 20–40 nm × 5–10 nm × 0.5–50 μm) were purchased from Sigma-Aldrich. Fibers were prepared by dielectrophoresis [97]. Briefly, the tip of a sharp tungsten wire was immersed into a droplet of a CNT suspension in water and a fiber of desired length was drawn under an AC voltage. Our set-up enables preparation of fibers up to 100 mm in length. By changing the concentration of the CNT suspension, the drawing speed, and the voltage, it is possible to vary the diameter of the fibers from submicron to 400 μm. A typical CNT-fiber used in our BSA adsorption experiments is shown in Fig. 14.

To assure the comparability of individual sensors, a precursor fiber several centimeters long was drawn and then cut into equal length pieces to ensure uniformity of diameter and other parameters within the set of different sensors.

Biosensors were made by gluing the CNT-fiber to one prong of the QTF ($F_{\text{res}}=32768$ Hz, Clock quartzes TC-38) using an epoxy glue (Eccobond 286, Emerson & Cuming).

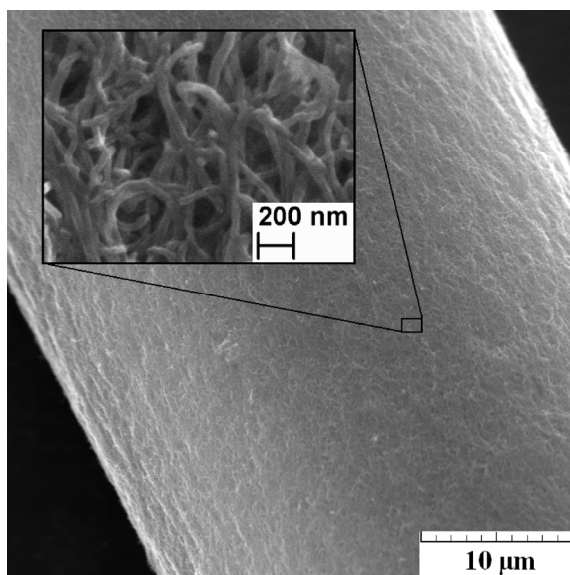


Figure 14. SEM micrograph of a CNT-fiber.

The principle of operation of a novel sensor consists in immersing only the CNT-fiber into the solution, while keeping the QTF above the liquid (Fig. 15). In this case, the CNT-fiber acts as an extension of the QTF's prong. Changes in the fiber's mass result in an immediate shift of the QTF's resonant frequency. During measurements, the QTF is driven electrically in self-excitation mode and frequency response is constantly monitored, thus providing real-time information on the adsorption rate. If previously calibrated, the sensor can measure the exact mass of the adsorbed substance. Proposed technique enables measurements in volumes as small as few tens of microliters.

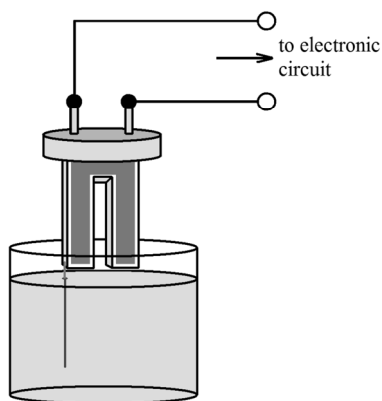


Figure 15. Schematic representation of the experimental set-up: CNT-fiber is immersed into an analyte solution, while QTF is kept above the liquid.

The BSA adsorption measurements included several steps. First, the sensor was conditioned by immersing the fiber into pure buffer solution for several minutes until slow diffusion of the liquid into its pores was completed. Diffusion of the solvent resulted in a decrease in the resonant frequency. Conditioning was considered finished when the resonant frequency stabilized. Then, the fiber was immersed in BSA solution and the shift in resonant frequency corresponding to the adsorption of BSA was monitored. Finally, the fiber was immersed into pure buffer again to determine whether the adsorption process was reversible. All experiments were performed at room temperature ($22 \pm 2^\circ\text{C}$).

Fig. 16 shows the typical frequency shifts for the 20 mm CNT fiber in 0.1 mg mL^{-1} BSA solution at two different pH values. It is evident that at pH 4.8, the adsorption rate of BSA is significantly higher than that at pH 7. The total frequency shift within 25 minutes was 4.5 Hz for pH 7 and 20 Hz for pH 4.8, respectively. The saturation time was approx. 10 min. After BSA adsorption measurements, the fiber was transferred to a pure buffer solution. No recovery of the initial F_{res} was observed, indicating that the BSA adsorption process was irreversible. These results are in good agreement with work by Valenti et al. [96], who studied the adsorption of BSA to CNTs by reflectometry. They found the adsorption of BSA to CNTs to be irreversible, and reported an approximately twofold difference in the adsorption rates for pH 4.8 and pH 7. The saturation time was also on the same order. According to their explanation, the pH-dependence of BSA adsorption is related to the conformations of the protein molecules and intermolecular electrostatic interactions. At the isoelectric point for BSA (IEP, pH 4.8), the compact structure and absence of lateral electrostatic interactions facilitate the adsorption of BSA to CNTs. On the other hand, the lower adsorption observed at a pH far from the IEP (BSA molecules are positively charged at pH lower than 4.8 and negatively charged at higher pH values) is mainly caused by increased intermolecular repulsion.

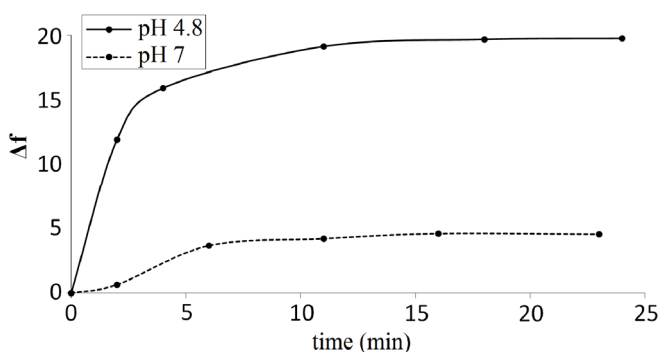


Figure 16. Typical resonant frequency shifts for 20 mm CNT fibers immersed into 0.1 mg mL^{-1} BSA solution at two characteristic pH values.

We found the performance of the sensor to be strongly dependent on the characteristics of the CNT-fiber. The fiber must have a porous structure to provide sufficient area for analyte adsorption. The pores must be large enough to enable the BSA molecules to travel in. The diameter of the fiber should be optimal: too thin or too thick fibers do not provide sufficient sensitivity, as thinner fibers are not stiff enough to transfer the vibration energy to the QTF, while in case of thicker fibers there is a high damping of oscillations due to the fluid resistance. The optimal length and cross-section of the fiber was found to be on the order of 20 mm and 30 μm , respectively. Shorter fibers provided lower sensitivity, while for longer fibers, no increase in sensitivity was observed. Apparently the oscillation does not propagate in the fiber further than 20 mm and the additional length of the longer fiber does not participate in sensing.

As the aim of our measurements was only to compare BSA adsorption rates at different pH values, no mass calibration of the sensors was performed and, hence, no information on the amount of the adsorbed BSA was extracted.

The method proposed here overcomes limitations for the use of QTF-based sensing in aqueous solutions while preserving main advantages of QTF over other resonance sensors like high q -factor, frequency stability, low price and simpler electronics.

6.2. Real-time manipulation of gold nanoparticles inside scanning electron microscope with simultaneous force measurement (Paper I)

The aim of the study described in this section was finding relation between frictional and structural properties of gold nanoparticles and elaboration of extended particle manipulation and frictional force measurements method in comparison to manipulation techniques described in chapter 3 by providing real-time observation of manipulation procedure. High sensitivity of QTF is applied here for detection of forces as small as few nN.

6.2.1. Experimental details

The 150 nm Au nanoparticles were purchased from BBI International. Oxidized silicon wafers (50 nm of thermal oxide) were purchased from Semiconductor Wafer, Inc. (Structural properties of gold nanoparticles, essential from tribological point of view, are reviewed in section 4). The samples were made by depositing droplets of an Au nanoparticles suspension onto the Si wafer. Samples were annealed for one hour at 725 K prior to every experiment to remove the surfactant and decrease adhesion. A Helios NanoLab (FEI) field emission microscope was used to characterize the samples before and after thermal treatment.

Force sensors were constructed in a manner similar to Rozhok et al. [29]. An AFM cantilever with a silicon tip (NT-MDT) or etched 0.1 mm W wire [98]

was glued to one prong of a commercially available QTF ($f_{\text{res}} = 32,768 \text{ Hz}$) using conductive silver epoxy (M.E. Taylor Engineering, Inc). Depending on the side to which the tip was glued, the sensor operated in normal or shear modes. In normal mode, the QTF oscillated perpendicularly to the surface in a manner similar to a conventional AFM (Fig. 17 a). In shear mode, the sensor oscillated parallel to the surface (Fig. 17 b, c).

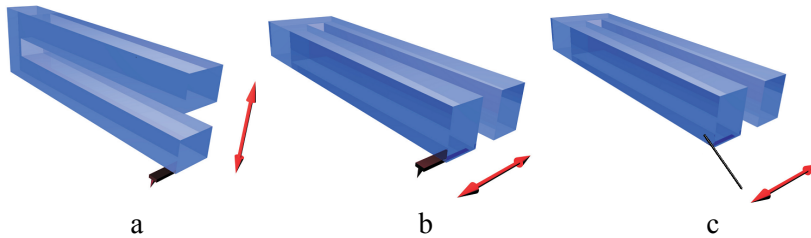


Figure 17. QTF with AFM tip (a and b) and W wire oscillating in normal (a) and shear (b and c) regimes.

Force measurements were based on the fact that the oscillation amplitude of the sensor oscillating on its resonant frequency depends on the forces acting on the tip. Sensor oscillations were excited by applying alternating voltage to its electrodes using a lock-in amplifier (SR830; Stanford Research Systems). The amplitude of free oscillations at the tip apex was on the order of 100 nm. The sensor also provided feedback to control the distance between the tip and the surface. For detailed description of the force measurements with QTF see chapters 1 and 2.

The force sensor was mounted on a 3D piezo nanomanipulator (SLC-1720-S, SmarAct) and installed inside an SEM (VEGA II, Tescan) (fig. 18). The SmarAct 3D nanomanipulator enables two types of movements: in single-line scan regime (hereinafter “scan regime”), the movements are made by expansion or contraction of the piezo to which the sensor is fastened. This regime provides an atomically smooth and accurate motion. In step regime, movements are made in a series of gradual expansions of the piezo followed by abrupt slips achieved by a sawtooth signal sent to the piezo positioner.

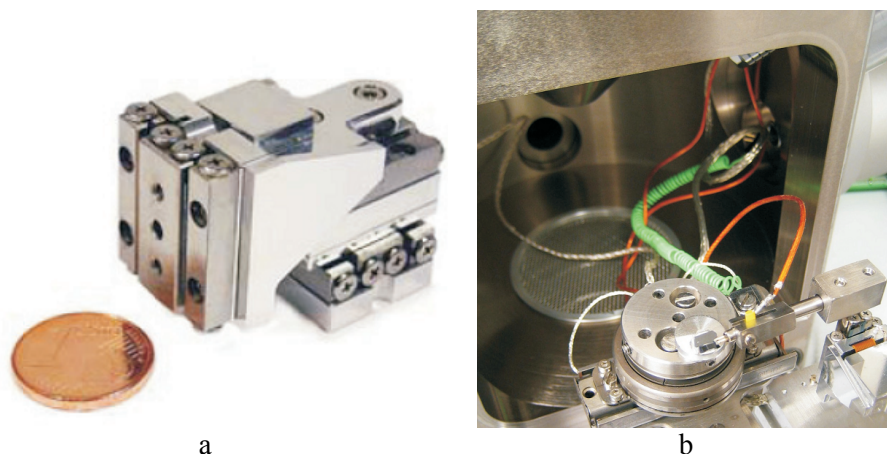


Figure 18. a) SmarAct 3D nanomanipulator. b) Photograph of the nanomanipulator with QTF force sensor installed inside SEM.

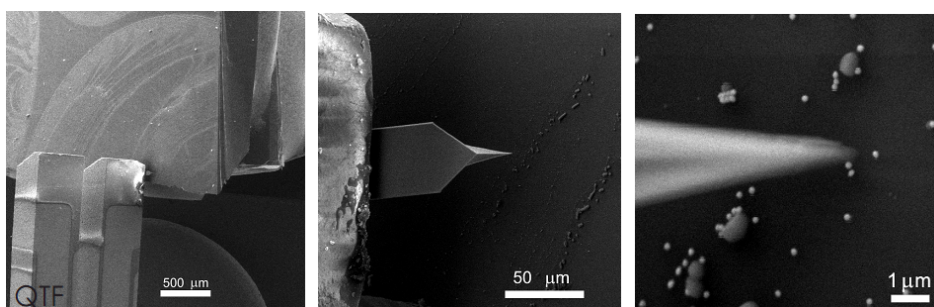


Figure 19. SEM micrographs of the force sensor above the substrate with Au nanoparticles in different magnifications.

When QTFs with AFM cantilevers were used, the sample and the sensor were tilted at 45 degrees relative to the table plane to enable visual control of the manipulation procedure (Fig. 20). Manipulation in this case was done only along the Y-axis to provide an approximately constant distance between the tip and the sample. In the case of tungsten wire, the tip protruded hundreds of μm from the QTF prong and was clearly visible without tilting.

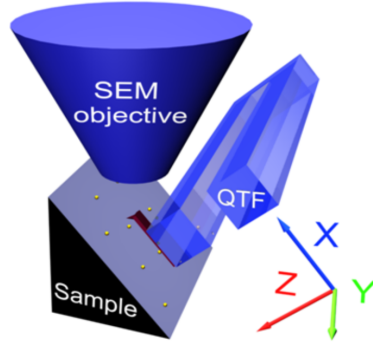


Figure 20. QTF and sample tilted at 45 degrees to the SEM objective

Thermal drift for given experimental set-up was on the order of 0.1 nm/sec and could thus be neglected within one manipulation event. Extensive custom software was developed for manipulation rather than using the standard SmarAct software.

All sensors were calibrated in both the Y and Z directions on reference contact AFM cantilevers [99] that had been previously calibrated by the thermal noise method [100]. Typical calibration curves are shown in figure 21. It is evident that in shear mode QTF is about 10 times more sensitive.

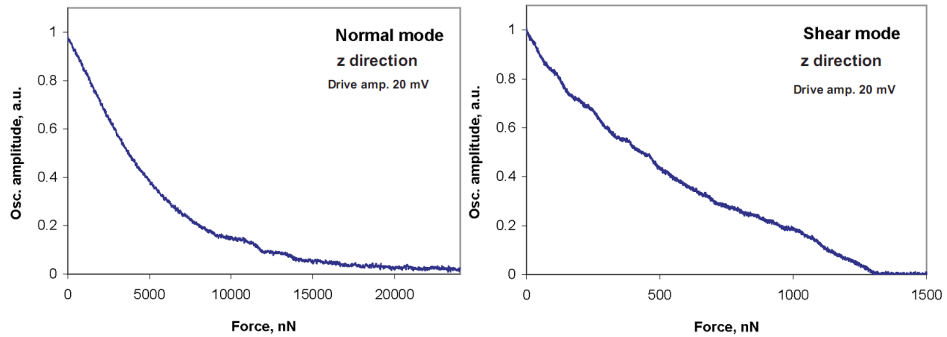


Figure 21. Force calibration curves for a) normal mode and b) shear mode.

To obtain a sufficient force resolution and sensitivity, the q-factor of the sensor should be high. The mass of the glued AFM cantilever is small in comparison to QTF and does not significantly alter the Q-factor of the QTF. The effect of the very thin glue film is negligible. However, when Q-factor is too high, the inertia of QTF is significant and QTF reacts too slowly to any rapid changes in force. This results in beat-frequency interference oscillations having the same order of amplitude with that of useful signal. Thus, when using amplitude modulation

strategy, Q-factor should be optimized (reasonably decreased) to find a compromise between adequate resolution and short response time. In our case this was implemented by adding small droplet of epoxy (Ecobond 286, Emerson & Cuming) onto one of the QTF prongs. Fig. 22. demonstrates the differences in reaction time to frequency change for unoptimized and optimized force sensor. In case of tungsten there is no need in optimizing the Q-factor because of the high mass of the tungsten wire.

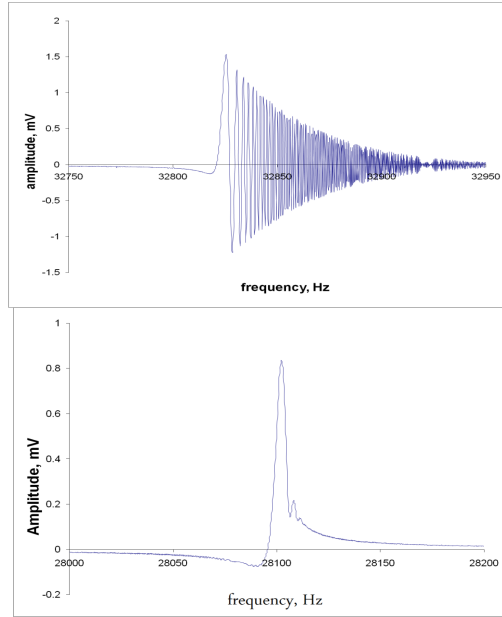


Figure 22. Frequency sweep around resonant frequency for unoptimized (left) and optimized (right) QTF force sensor. Driving voltage and the scan time are the same for both cases. Unoptimized QTF gives higher output signal, but beat-frequency interference oscillations are generated. Output signal of optimized QTF is only 2 times lower, however response is many times faster.

6.2.2. Measurements of static friction during manipulation of nanoparticles

For manipulation experiment, the tip was brought into the close proximity to the chosen particle. The particle was then displaced (“kicked”) from its initial position by an abrupt tip motion in the step regime to reduce the initial adhesion [47], which is known to be time-dependent [101], to its minimal value. Initial displacement was followed by controlled manipulation of the particle by pushing it with the tip in scan regime with simultaneous force recording. During manipulation, the tip moved parallel to the surface along a straight line without feedback.

Fig. 23a presents a typical manipulation curve for the QTF oscillating in normal mode. The initial flat region **A-B** of the curves corresponds to the movement of the tip above the surface. Decline of the curve at region **B-C** was caused by a long-range interaction between the tip and the particle. The abrupt drop in amplitude at **C** corresponds to the force needed to overcome the static friction and displace the Au particle from its initial location. When static friction was overcome, the particle jumped in the direction indicated by the arrow. From **D** to **E**, the particle moved smoothly with the tip. For the moving particle, the amplitude drop was only few percent lower than it was before contact.

Fig. 23b shows a manipulation curve for the QTF oscillating in shear mode. The initial flat region from **A** to **B** of the curve corresponds to the movement of the tip at a constant set point above the surface. The abrupt drop in amplitude from **B** to **C** corresponds to the force needed to overcome static friction and displace the Au particle. The particle made a small jump in the direction indicated by the arrow. From **D** to **E**, the particle moved smoothly with the tip, and minor oscillations related to tip-particle interaction were noticeable.

In all manipulation experiments, the tip moved in the *Y* direction. We used the *Y*-direction force-calibration data to convert amplitude to force (further details are given below). Values of static friction ranged from 40 to 450 nN for normal mode and from 50 to 750 nN for shear mode. It should be noted that the oscillation amplitude often dropped to zero. This drop corresponds to a force higher than 1,500–2,500 nN (the upper limit depending on the particular sensor). Forces higher than these limits could not be measured due to the limited range of QTF sensitivity at a given driving voltage.

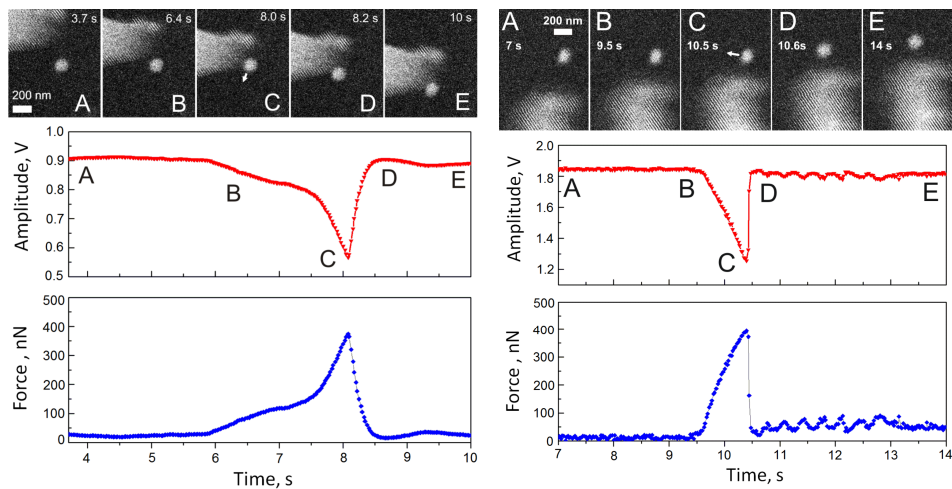


Figure 23. Snapshots of the manipulation process and corresponding amplitude and force curves, normal (a) and shear mode (b).

Fig. 24 displays a distribution histogram of the static friction forces for the manipulation experiments in normal and shear modes. The static friction values for the cases when the amplitude dropped to zero remain unknown and thus could not be included in the histogram.

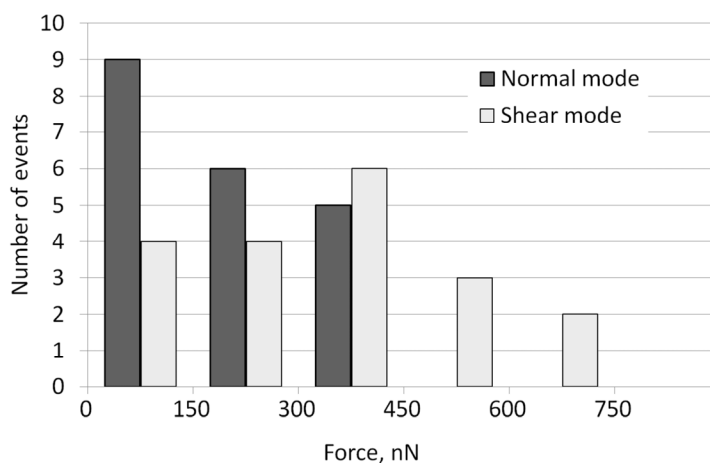


Figure 24. Distribution of static friction forces based on 20 manipulation events in normal mode and 17 manipulation events in shear mode.

From the experimental results, it is evident that considerable force is needed to overcome static friction in this system. However, once the threshold for static friction was exceeded and the particle moved smoothly with the tip, then only minor changes in oscillation amplitude were observed in a few cases. Most of kinetic friction values were below the detection limits of our setup. This finding is in agreement with other researches, who have demonstrated that kinetic friction is vanishing for clean surfaces in vacuum [102].

Variations in the experimental values of static friction may be due to the fact that the contact area between a particle and a substrate can vary due to deviations from a spherical shape. From Fig. 25a it is clearly seen, that Au particles used in the experiment were, in general, not spherical and had facets of different sizes.

Geometrical factors may also play a crucial role in the reduction of static friction after a thermal treatment. In our experiments, the main reason for heating the samples was to burn out the surfactant remaining after the deposition of the particles onto substrate. However, it was found that annealing at 773 K also led to a rounding of the particles (see Fig. 25b), which, in turn, should result in reduction of contact area and static friction.

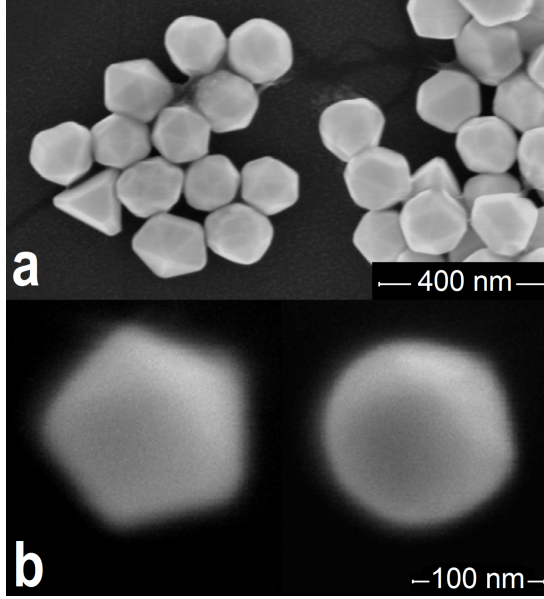


Figure 25. (a) Au particles of different shape as deposited from solution. (b) SEM micrograph of the same Au particle before and after annealing for 1 h at 773 K.

Here, analytical estimation of the static friction considering the geometric parameters [103] of the particles used in our manipulation experiments is provided. It has theoretically proposed and experimentally proven that friction at the nanoscale is proportional to the contact area: $F_{frict} = \tau A$, where A is the contact area and τ is the shear strength [104].

For spherical particles, the contact area can be calculated on the basis of continuum elasticity models for deformable spheres [47] such as the Johnson-Kendall-Roberts (JKR) model [105] or the Derjaguin-Muller-Toporov (DMT) model [106]. According to Tabor [107], the choice of the most suitable model is determined by the parameter:

$$\eta = \left(\frac{16R\gamma^2}{9K^2z_0^3} \right)^{1/3}, \quad (6.2.2.1)$$

where R is the radius of the sphere, γ is the work of adhesion, and z_0 is the equilibrium spacing for the Lennard-Jones potential of the surfaces. K is the combined elastic modulus of the sphere and substrate defined as $K = \frac{4}{3}[(1-\nu_1^2)/E_1 + (1-\nu_2^2)/E_2]^{-1}$ in which $\nu_{1,2}$ and $E_{1,2}$ are the Poisson ratios and

Young moduli of the substrate and sphere, respectively.

Assuming the following parameters for silicon and gold: $E_1 = 71.7$ GPa, $\nu_1 = 0.17$, $E_2 = 78$ GPa, $\nu_2 = 0.44$, $\gamma = 50$ mJ/m² [47], $R = 75$ nm and $z_0 = 0.3$ nm, we

obtained $\eta = 0.158$. For small η , the DMT-M theory is more appropriate [107]. According to the DMT-M model, the contact area

$$A_{DMT-M} = \pi \left(\frac{2\pi\gamma}{K} \right)^{2/3} R^{4/3}. \quad (6.2.2.2)$$

for spherical Au NPs with $R = 75$ nm is $A_{DMT-M} \approx 31.43$ nm².

The contact areas of the faceted NPs can be easily calculated using geometrical considerations. The results of the calculations for tetrahedral, decahedral and icosahedral NPs are presented in Table 1.

The shear strength τ can be estimated using the relation $\tau_{theo} = G^* / 30$ between the theoretical shear strength and the combined shear modulus, $G^* = [(2 - \nu_1) / G_1 + (2 - \nu_2) / G_2]^{-1}$, where $G_{1,2} = E_{1,2} / 2(1 + \nu_{1,2})$ [108, 109]. The ultimate static friction can then be calculated as $F_{frict} = \tau_{theo} A_{DMT-M}$.

Table 1. Estimated static friction forces for 150 nm Au particles of different geometries.

Shape	Contact area, nm ²	Static friction, nN
Spherical	31	9
Tetrahedral	9,743	2,768
Decahedral	3,652	1,038
Icosahedral	2,693	765

It should be noted that the geometry of real particles is more complex due to the presence of arbitrarily truncated edges and apexes (Fig. 25a). Thus, the contact areas and static frictions should generally be lower than the maximum values listed in Table 1.

According to the histograms (Fig. 24), low static friction force values prevail in the obtained data set. This finding can be interpreted as a reduction of contact area due to shape evolution towards the spherical after thermal treatment. For values beyond the upper detection limit (where the amplitude dropped to zero), the geometry was assumed to be highly faceted.

The displacement of strongly adhered particles entails the risk of their plastic deformation. As one of the main objectives of present study was to compare the normal and shear modes, measurements were narrowed to the low-friction region.

Normal oscillation mode is commonly used for the AFM manipulation of nanoparticles. Considering that friction is significantly higher at ambient conditions than in vacuum [102], our results correlate well with the previously reported static friction values of 130 nN for 15 nm Au nanoparticles on poly-L-lysine coated mica in air [110]. In many studies, the friction was estimated from

the dissipated power [46]; however, the data obtained using such an approach do not allow for comparison with direct frictional force measurements.

In normal mode, the sensor oscillated perpendicularly to the sample plane, producing a horizontal force component determined by the contact angle (Fig 26). The use of a nonzero contact angle requires sensor calibration in both the horizontal and vertical directions. However, according to our calibration data, the sensor was about ten times less sensitive in the Z (vertical) direction than in the Y (horizontal) direction. The ratio between the vertical and horizontal components of the applied force remains unknown, as it is determined by the contact angle, making interpretation of recorded signal in normal mode complicated. The vertical component applies load to the particle and increases the friction.

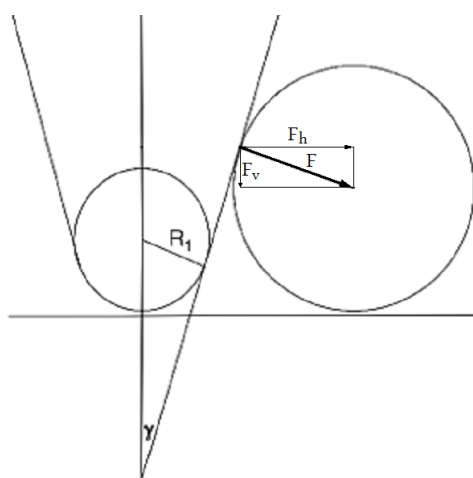


Figure 26. Contact point between the tip and the particle

In shear mode, the tip oscillated parallel to the sample plane, and the alternating vertical component was almost absent (the small value may be due to imperfect alignment of the sensor with the sample). The force calibrations in both the Y and Z directions showed the same sensitivity within the accuracy of our measurements.

The manipulation curves for both normal and shear oscillation modes were rather similar. However, the values of static friction measured in normal mode were a few hundred nN lower than those measured in shear mode. This difference may be due to the contribution of the unaccounted vertical component in normal mode.

Normal mode is closely related to tapping mode and hence provides a stable setpoint. In shear mode, the tip oscillates above a certain area and it is more difficult to maintain a stable set point.

6.2.3. Influence of impact velocity

The influence of the impact velocity on the initial displacement of the particles is another challenging issue. The step regime was found to be more effective for the initial displacement of the particles than the scan regime. This might be related to the abruptness of motion in this regime; the tip strikes the particle with a much higher velocity than in scan regime. Visual information concerning the real motion of the tip and the particle is restricted by the scanning speed of the SEM. Manipulation events in the step regime are so fast that one can see only the initial and final positions of the tip and the particle and have no data on motion in between these points.

To simulate a step event in the scan regime, the scanning speed was increased. The initial displacement of stuck particles was impossible below a certain threshold. The increase of the scan speed up to 5 $\mu\text{m}/\text{sec}$ enables moving the particles more easily. Moreover, if the particles were often plastically deformed and smeared along the surface in the case of a slow impact, then at high tip velocities, the particles moved as a rigid entity. This result suggests the possibility that the viscoelastic properties of Au particles may depend on impact velocity; however, additional experiments are required to determine if this is the case.

6.2.4. Aging of contact between nanoparticle and substrate.

Considerable sticking of Au particles to oxidized Si substrate exposed to ambient condition was observed. Sticking increases with time significantly and after two months being exposed to air it was impossible to move any particle. Similar sticking behavior for Sb particles on HOPG exposed to air was reported Dietzel et. al [51].

In present work it was found that after annealing the sample at 725 K for 1 hour particles moved easily again. However, annealing solves the sticking problem only until the next long term exposure. Several exposure-annealing cycles for the same sample revealed that the process is reversible. Actual nature of this phenomenon is still not clear, whether it has chemical (catalytical activity of nanosized gold) or physical nature (diffusive rearrangement of gold atoms in contact area).

6.2.5. Deformation of Au nanoparticles

For the Si and SnO_2 samples exposed to ambient condition for two months the adhesion was higher than the energy needed to bend the tungsten tip or damage the AFM tip. In case of Au the deformation of the particles was observed instead of displacement (fig. 27). The deformation threshold can be found either from the amplitude drop or from the torsional deflection of the cantilever that can be easily registered visually during manipulation.

Deformation threshold was found to be rate indentation rate dependent. At low velocities particles were smeared, at high impact velocities particles were translated as a whole.

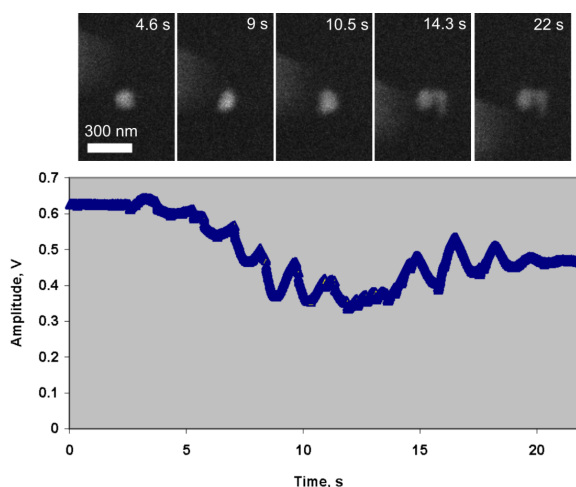


Figure 27. Deformation of 150 nm Au nanoparticle stuck to substrate, scan regime, normal mode.

6.3 Real-time measurements of frictional and mechanical properties on ZnO nanowires inside SEM (Paper VI)

In this section, real-time manipulation technique is proposed, which enables measurement both elastic and frictional properties of the same NW on a flat substrate inside SEM. ZnO NW was translated over a surface of an oxidized silicon wafer using nanomanipulator equipped with force sensor, composed of QTF force sensor, described in details in previous sections. Elastic deformation of translated NW was used to determine distributed kinetic friction force. Same NW was then positioned half-suspended on an edge of trenches cut by focused ion beam (FIB) in silicon wafer. In order to measure Young modulus NW free end was pushed laterally by AFM tip, and interaction force corresponding to visually detected NW bending was measured by QTF force sensor. No gluing or welding of NW was used in these experiments, enabling to preserve NW unchanged and disposable for other experiments. Proposed approach enables to reduce uncertainties in measured friction caused by use of bulk value of Young modulus or averaged value of Young modulus measured on a set of NWs, providing Young modulus measured for each particular NW.

The use of QTF with glued AFM tip as a probe and force sensor has some advantages in comparison to application of soft contact mode AFM cantilever for investigation of NW mechanical and frictional properties inside SEM. QTF provides real-time data flow of NW-tip interaction with high time and force resolution. Moreover, QTF force sensitivity can be tuned in wide range by variation of applied driving voltage. High force constant in order of 10-20 N/m of AFM cantilever glued to QTF force sensor enables easy manipulation of

highly adhered NW or NPs on substrate surface [111], which may be problematic if soft AFM cantilevers are used as probes [112].

6.3.1 Experimental details

For the present study the same manipulation set-up described in 6.2 was used. Tip of *AdvancedTEC* AFM probes (*Nanosensor* ATEC-CONT cantilevers $C=0.2$ N/m) used in experiments is tilted about 15 deg relative to cantilever, providing tip visibility from top.

ZnO NWs were grown by vapor transport method using Au NPs (*BBI international*, 60 nm) as catalyst [113]. NWs were grown on silicon substrates by heating a 1:4 mixture of ZnO and graphite powder to 800-900 °C in open-end quartz tube during 30 min. Obtained in such way NWs have hexagonal cross-section.

An array of 1 μm deep trenches of sizes 3x3 μm and 1x3 μm was cut by FIB (*FEI Helios NanoLab*) in Si wafer (50 nm of thermal SiO_2) (fig. 28 a, b). Wafers were cleaned with RCA-1 solution (or “standard clean-1”), followed by 12% HCl, rinsed with distilled water and blown with nitrogen. Nanowires were transferred from original substrate onto FIB patterned wafer surface using piece of cleanroom paper.

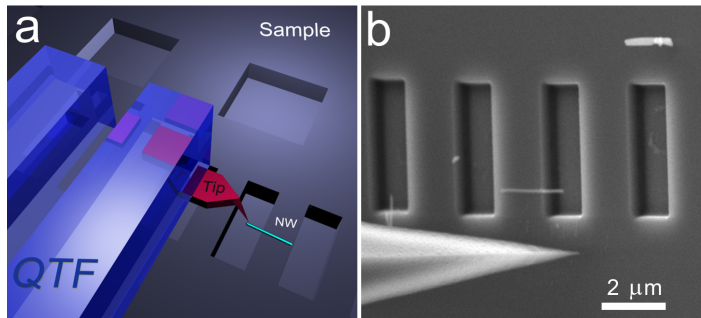


Figure 28. Schematics of experiment (a). QTF with glued AFM tip approached to a NW suspended over a trench on silicon sample. Corresponding SEM image of AFM tip and FIB cut trenches (b).

NWs of suitable length in order of few μm and situated in proximity of patterned area were chosen and moved by AFM tip towards trenches cut by FIB. To increase loading during the NW translation and ensure the tip will not slide over NW, the force sensor was lowered another 1-2 μm after the tip came into contact with the substrate surface. Oscillation amplitude drops to zero due to high repulsive force, and no force measurement performed during NW translation.

When the NW pushed at its midpoint has traveled over few microns, it bends into an arc due to the distributed kinetic friction force q_{kin} (kinetic friction

divided by the NW length) acting along the NW's length (fig. 29). Its characteristic shape remains constant during the following translation due to the fact, that total kinetic friction force acting on the NW is balanced with the external force applied by tip. Determination of distributed kinetic friction for too short NWs was problematic due to large radius of curvature during translation. Minimal length suitable for determination of kinetic friction depends on NW's diameter and usually is at least 2 μm in our experiments.

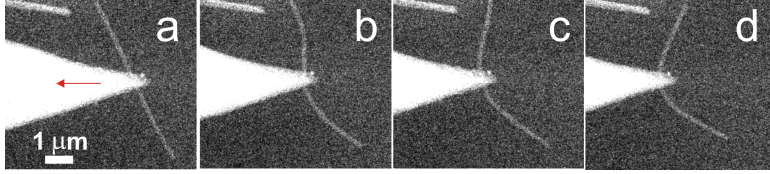


Figure 29. Evolution of NW shape profile during perpendicular to NW axis dragging. Intact NW. The arrow indicates the direction of tip movement (a). Partially displaced NW (b). Completely displaced NW (c). Final characteristic shape (d).

Timoshenko beam theory [108] was applied to calculate NW bending profile during its translation with the method described in [114] (*see appendix*). The NW shape is then described by a differential equation of equilibrium of the NW on the interval $(0, L)$ [111]:

$$IE \frac{d^2 \varphi}{dl^2} = -q_{kin} l \sin \varphi + F_{apl-lat} H\left(l - \frac{L}{2}\right) \quad (6.3.1.1),$$

where E is the NW Young modulus, I is the area moment of inertia of the NW (for hexagonal cross-section $I = (5a^4 3^{1/2})/16$ where a is a side length of hexagon), L is the NW length, and φ is the angle between the tangent line of the NW and the direction of motion as a function along the nanowire axis l and $H(x)$ – Heaviside step function. $F_{apl-lat}$ is the lateral component of the applied force, which depends on applied force F_{load} through the contact angle α [115]:

$$F_{apl-lat} = F_{load} \cdot \text{ctg}(\alpha) \quad (6.3.1.2).$$

For more details see manuscript [116] in appendix.

This equation 6.3.1.1 can be solved numerically and the obtained profile can be compared to the experimentally obtained NW profiles (figure 29).

Considering the NW length L , diameter D , measured Young modulus E and NW profile shape experimentally obtained from SEM image one can estimate the distributed kinetic friction force q_{kin} by fitting the values into eq. 6.3.1.1. Young modulus measurement procedure will be described below.

Measurements were carried out on five NW of different diameter. Interfacial shear stress σ_{kin} , which is considered to be a fundamental property of nanoscale friction ($F_{friction} = \sigma A$), where A is the contact area (assuming a hexagonal cross section $A = LD / \sqrt{3}$), can be calculated as $\sigma_{kin} = q_{kin} \sqrt{3} / D$ [117]. Results are presented in Table 2. Average value of interfacial shear stress is $\sigma_{kin} = 2.1 \pm 0.26$ MPa. Results are in good agreement with 1 MPa value of interfacial shear stress obtained by Manoharan et al. for ZnO 30-40 μm long NWs of 200 nm in diameter for parallel to NW axis dragging [70].

Table 2. Kinetic friction and Young modulus of ZnO NW.

Nr.	Diameter, nm	Length, nm	q_{kin} , nN/nm	σ_{kin} , MPa	Young modulus, GPa
1	112	3850	0.115	1.8	38
2	125	3280	0.135	1.9	58
3	160	3140	0.2	2.2	27
4	180	4640	0.25	2.4	41
5	230	4615	0.3	2.3	38

To determine NW's Young modulus the NWs were positioned on an edge of FIB cut trenches as it was shown on fig. 28 and 30. One end of NW was suspended over the trench, and another end was kept fixed to the substrate surface by strong adhesion force. The suspended part of NW was pushed by AFM tip during manipulator continuous movement (scan regime) parallel to the trench wall (fig. 30). QTF oscillation amplitude signal, which directly correlates with the applied force, and grabbed SEM images were recorded simultaneously during experiment. In our experiment the length of suspended part of NW is about 1 μm in contrast to at least few tens μm in other works of NW bending [70, 118]. It gives possibility to measure Young modulus of rather short NW.

It is necessary to note, that region close to the trench (approx. 250-500 nm) is slightly concave due to not perfect focusing of ion beam. That causes an increase of NW suspended part L (shifted rightward relatively to trench wall). Suspended part of NW looks more transparent in comparison to adhered part (fig. 30 b, c).

The equation of equilibrium for purely bent elastic beam with Young modulus E and I momentum of inertia being loaded by a point force f at its end can be written as [108, 111]:

$$E \cdot I \cdot \frac{d^2\theta}{dl^2} + f \cdot \cos\theta = 0, \quad (6.3.1.3)$$

where l is the natural axis of the NW, θ is the angle between tangent of the bent NW profile projected on initial nanowire profile, L is the length of suspended part of NW. The equation can be solved numerically or expressed in elliptic functions with the boundary conditions:

$$\begin{aligned} \theta|_{l=0} &= 0 \\ \frac{d\theta}{dl}\bigg|_{l=L} &= 0 \end{aligned} \quad (6.3.1.4 \text{ a, b})$$

Eq. (6.3.1.4) implies that the NW is fixed along its axis in the adhered part, and Eq. (6.3.1.4 b) is dictated by absence of momentum at the end of NW. In order to find the value of Young modulus SEM image of NW profile was numerically fitted to the curve given by Eq. (6.3.1.3) (fig. 30c).

Typical force curve and corresponding SEM images are presented in fig. 30. Young modulus for this wire was found to be 58 GPa. Characteristic shape of NW during dragging before it had been positioned on the edge of trench is shown on inset. Distributed friction force and kinetic friction shear stress were found to be 0.14 nN/nm and 1.9 MPa respectively.

We found averaged value of Young modulus 40.4 ± 11 GPa (table 2). The mean value is in good agreement with other works performed on ZnO NWs: Manoharan et al. found 40 GPa for NW of diameter 200-750 nm [70], and Song et al. referred 29 GPa for NW of average diameter 45 nm [112].

Significant variation in magnitudes of Young modulus from 27 to 58 GPa in the measured set of NWs makes an importance of gathering Young modulus for each NW individually evident in order for calculations of kinetic friction based on the balance of elastic and friction forces. Variation in sliding friction and shear stress values was of order of magnitude for InAs NWs [79], probably due to usage of bulk modulus of InAs in such calculations. In our experiment standard error was about 12% of the mean value of kinetic shear stress. Thus, the use of individual values of Young modulus is able to make friction force and shear stress determination more reliable.

In most bending experiments adhered part of NW remained motionless. It means that applied force was lower than static friction force between NW and substrate. NWs were never broken during bending experiment even at large bending angles ($\theta \approx 60^\circ$). During bending the NWs were undergone a pure elastic deformation, however in few cases NWs were broken by tip in abrupt motion (step regime), when tip was close to a trench wall.

It was possible to displace as a whole only NWs having high Young modulus and / or very short part adhered to substrate (fig. 31). We avoided positioning the tip closer to trench wall due to the risk of touching the wall and introducing artefacts to the force curve. Maximal force of $F=1620$ nN was detected before adhered part of NW of length $l=550$ nm was displaced, which corresponds to averaged static friction force $q_{st}=F/l=3$ nN/nm.

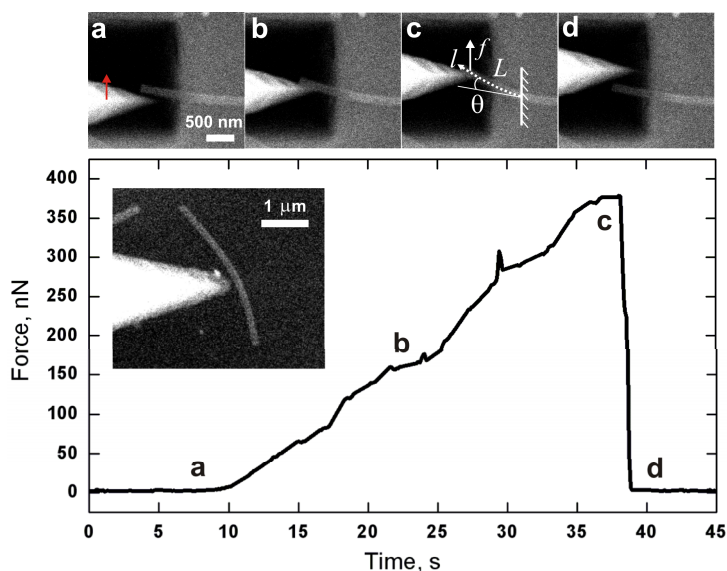


Figure 30. SEM images of suspended NW being pushed by tip and corresponding force curve. Tip approaches to NW. The arrow indicates the direction of tip movement (a). NW is slightly bend (b). Maximal bending of NW and corresponding schematics of NW loading laid over the SEM image (c). NW came off the tip. Force drop to zero (d). Inset: characteristic shape of the same NW dragged by tip over sample surface before been positioned on trench edge. Calculated Young modulus and friction force are $E=58$ GPa and $q_{\text{kin}}=0.14$ nN/nm respectively.

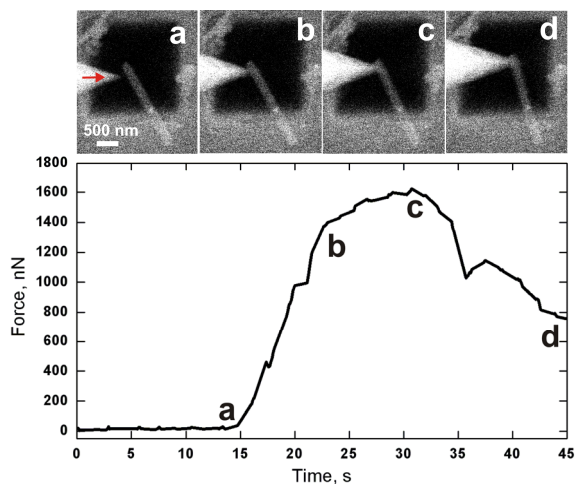


Figure 31. SEM images of full displacement (rotation) of NW. Tip approaches to NW. The arrow indicates the direction of tip movement (a). Tip contacts NW (b). NW starts to slide (c). NW was rotated (d). Averaged static friction force is $q_{\text{st}}=3$ nN/nm. Absence of noticeable elastic deformation did not allow determination of Young modulus.

Proposed approach also opens a route to measure Young modulus and the maximal static friction force of the NW having adhered part long enough to keep the NW fixed to the substrate. The procedure consists in sequential shortening of the adhered part of the NW by FIB followed by pushing the NW with an AFM tip until the whole NW is displaced.

6.4. Crystal mismatched layers in pentagonal nanorods and nanoparticles (Papers II and III)

Pentagonal symmetry is frequently occurring in the world on NPs (Fig. 32). First observed for FCC crystals such as Au, Ag, Cu, it was then reported for other materials [119]. Pentagonal crystals and particles can be obtained via physical or chemical vapor deposition on various substrates, homogeneous nucleation in inert gas atmosphere, electrodeposition, growth from melt, metal colloid precipitation, sol-gel techniques and even precipitation from solid solutions [119]. In present study gold NPs obtained by colloidal method were used for experimental observation of geometry. Method is based on reduction of Au ions in a mixture of tetrachloroauric (III) acid hydrate ($[\text{HAuCl}_4] \cdot \text{H}_2\text{O}$) and trisodium citrate. By reducing the HAuCl_4 with trisodium citrate, stabilized nanoparticles, which bear the negative charge of the citrate ions, are obtained. The average size of the obtained nanoparticles can be controlled during reaction by temperature, steering, or chemically by adding appropriate chemicals like NaBH_4 and can range from several nm to tens and hundreds of nm. Moreover, the shape of nanoparticles can also be adjusted by varying the reaction conditions and addition of appropriate surfactant [120].

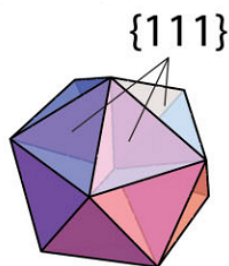


Figure 32. Icosahedral pentagonal NP.

Pentagonal nanoparticles (PNPs) and nanorods (PNRs), as well as their larger micrometer-size relatives, have internal elastic strains with corresponding mechanical stresses [121, 122]. As a result of internal straining PNRs and PNPs possess stored elastic energy proportional to the volume of the PNR (or PNP). This energy can be diminished in the course of relaxation processes in PNRs (PNPs) accompanied by the formation of various defects, e.g., dislocations, disclinations, pores etc. [121, 123]. (Stresses and stress release mechanisms for

nanoparticles in general are reviewed in chapter 4.) It also known that physical properties of small nano-size particles can be essentially modified by the formation of a shell (or coat) layer covering the surface of a nanoobjects [122]. Therefore the question arises how such covering layers can modify the onset of mechanical relaxation processes in nano-size particles and rods.

In these two papers pentagonal nanoparticles (PNPs) and nanorods (PNRs) are theoretically and experimentally investigated and new mechanism of stress relaxation based on formation of shell layer with crystal lattice mismatch is proposed (fig. 33).

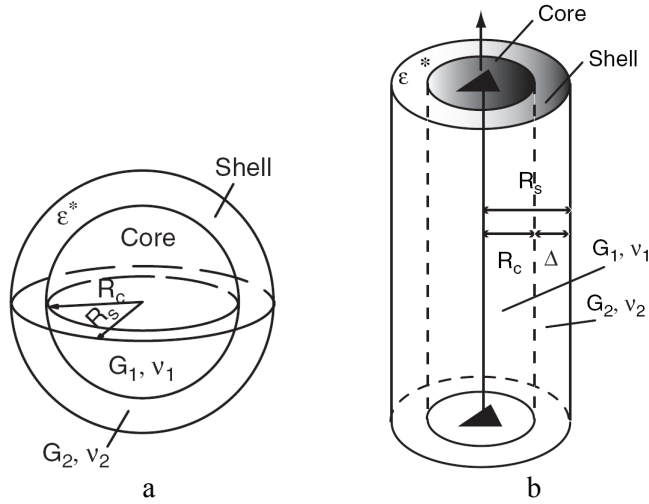


Figure 33. Formation of shell layer with crystal lattice mismatch in pentagonal nanoparticle (a) and nanorod (b). G_1, ν_1, G_2, ν_2 are the shear modules and Poisson's ratios of the core and shell correspondingly; R_c and R_s are core and shell radii and ϵ^* is a lattice misfit parameter.

Mechanical stresses and elastic energies of core-shell PNRs and PNPs are calculated and analyzed in the framework of linear isotropic elasticity. Difference between elastic modules of core and shell is taken into account. The threshold radii as the minimal radii of PNR and PNP for which the formation of the shell layer is energetically favorable are found to be approximately 10 nm for PNPs and 100 nm for PNRs of typical FCC metals. The optimal magnitudes of mismatch parameter giving the maximal energy release for shelled PNRs and PNPs are determined. For calculation details please refer to papers II and III [124, 125].

6.5. Method of cleaning the tip of atomic force microscopy (Patent IV)

As was already mentioned above, besides its main application in microscopy, AFM is also a most commonly used tool for nanomanipulations. In the framework of the thesis AFM tip is used in creation of QTF-based force sensors described in sections 6.2 and 6.3. AFM tip contamination problem and existing AFT tip cleaning methods are discussed in chapter 2.

Here, a novel AFM tip cleaning technique is described, which was elaborated with a purpose of enabling cleaning to be performed in situ without taking AFM cantilever out or moving it from its position above the substrate in contrast to existing cleaning methods reviewed in chapter 2. Cleaning of the AFM tip is performed directly in the place of the measurement of the substrate. The method is based on the conditions that the cleaning agent is condensed to the examined object for example in the form of carbon dioxide snow. The possible realization of the set-up for cleaning is shown schematically in figure 34. Using the abrasive properties of the carbon dioxide snow the tip is scanned over the examined surface whereas the contaminants are removed from the tip. After cleaning scan cycle the tip is heated quickly and the cleaning agent is vaporized together with contaminants (fig. 35 a and b). Cleaning in such way enables to continue scanning process from exactly the same position. Measurements can be continued after cleaning from the same position on the substrate.

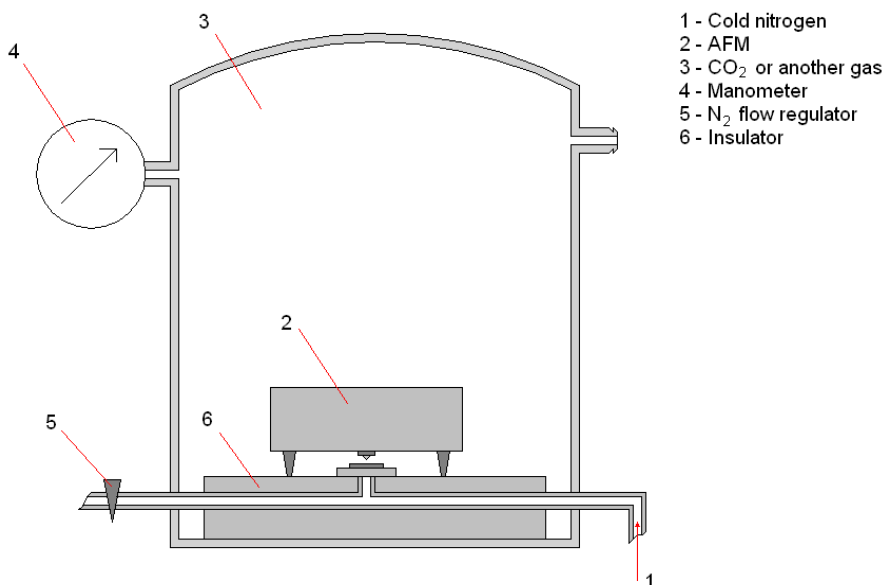


Figure 34. Set-up for cleaning the AFM tip.

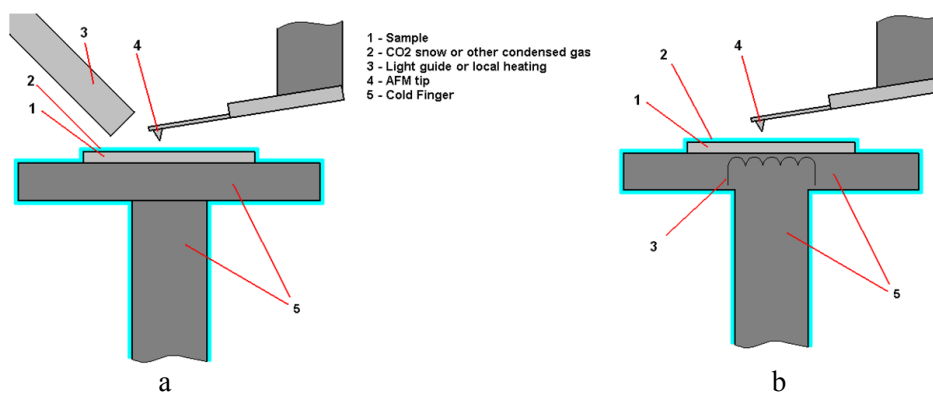


Figure 35. After cleaning scan cycle the tip is heated locally either by light guide or electrically.

SUMMARY AND CONCLUSION

A number of important problems concerning mechanical properties and behavior of nanostructures were assigned and treated within the framework of the thesis. Main activity and the novelty of the results are summarized below.

A method for real-time manipulation of nanostructures inside a scanning electron microscope (SEM) with simultaneous force detection, as well as appropriate equipment and software were elaborated. The method was applied for the manipulation and measurements of the frictional and mechanical properties of gold nanoparticles (NPs) and ZnO nanowires (NWs). Force detection was performed with a force sensor consisted of an atomic force microscope (AFM) tip glued to one prong of quartz tuning fork (QTF). Manipulation and measurements were performed in both normal and shear oscillation modes. Shear mode is found to be more sensitive and provide more straightforward interpretation of the results. Normal mode has more stable set-point, however there is an unaccounted vertical force component is present, which introduces uncertainties in results. Relations between the morphological and frictional properties of NPs were investigated. The influence of the thermal treatment on frictional properties of gold NPs was considered. Results for gold NPs are published in an international journal.

The frictional properties of NWs were measured from the profile of NW dragged at its middle point on a flat substrate. In this case the NW profile is determined by balance of frictional and elastic properties. Such approach requires knowledge of the Young modulus of NW. For the measurements of the Young modulus, NWs were put half-suspended on a trenches cut by focused ion beam (FIB) and bent by force sensor with simultaneous force measurements. Method provides Young modulus measured for each particular NW and therefore reduces the uncertainties in measured friction caused by the use of bulk or averaged value of Young modulus. No gluing or welding of NW is involved, enabling to preserve NW unchanged and disposable for other experiments.

In addition to the experimental measurements, NPs were also treated theoretically. A new mechanism of stress relaxation in pentagonal nanorods and nanoparticles was proposed and an appropriate model was developed. It was shown that for pentagonal nanoparticles and nanorods formation of a shell layer with crystal lattice mismatch could diminish the internal energy. The optimal mismatch parameter giving the maximal energy release, as well as the minimal radius of nanorods or nanoparticles, for which the formation of the layer is energetically favorable, were determined. The results are published in two international journals.

An unique atomic force microscope tip cleaning technique enabling cleaning to be performed in situ without taking the AFM cantilever out or moving it from its position above the substrate was elaborated. The method is based on the conditions that the cleaning agent (CO_2) is condensed to the examined object in the form of snow. Using the abrasive properties of the CO_2 snow the tip is

scanned over the examined surface whereas the contaminants are removed from the tip. Measurements can be continued after the cleaning from the same position on the substrate. The method is patented.

In addition, a novel method and an appropriate sensor for *in situ* tracking of the adsorption kinetics in aqueous solution was elaborated. The sensor comprises of a carbon nanotube (CNT) fiber attached to one prong of the quartz tuning fork (QTF). The method involves advantages of quartz tuning fork (QTF) over other sensors and overcomes the limitation of QTF applicability in aqueous solutions. The performance of a sensor was experimentally demonstrated by monitoring the adsorption of bovine serum albumin (BSA) at two different pH values corresponding to minimal (pH 7) and maximal (pH 4.8) BSA adsorption rates. By proper chemical treatment of the CNT-fiber the sensor can be developed to target specific biological molecules. The method is patented and experimental details are submitted in form of scientific paper.

Novelty of results

- For the first time applicability and peculiarities of normal and shear oscillation modes in terms of manipulation of nanostructures are compared and opposed.
- The relations between morphology and frictional properties for gold nanoparticles manipulated on oxidized silica substrate inside SEM are shown. Reduction of static friction after thermal treatment is demonstrated for gold nanoparticles at temperatures much below melting point of gold.
- An original method for real-time measurements of both elastic and frictional properties of the same NW is elaborated.
- A novel model of the stress relaxation in pentagonal nanoparticles and nanorods based on the formation of shell layer with crystal lattice mismatch is presented.
- A novel *in situ* AFM tip cleaning technique, which involves abrasive properties of CO₂ snow and eliminates the need to remove the tip from its position above the sample, is elaborated.
- A novel method and corresponding device for tracking adsorption kinetics in aqueous solutions *in situ* is elaborated.

SUMMARY IN ESTONIAN

Nanostruktuuride uuringud nanoskaalas vastastikmõjude ja mehaaniliste omaduste väljaselgitamiseks kasutades helihargi tüüpi kvartsresonaatorit

Väitekirjas käsitletakse mitmeid nanomõjudude tunnetuslikke aspekte nanotriboloogias, nanomehaanikas ja biosensoorikas. Selle multidistsiplinaarse töö kõiki osasid ühendavaks läbivaks eesmärgiks on nanointeraksioonide olemuse selgitamine. Tehnoloogia üldise miniaturiseerimistrendi valguses on väga oluline mõista nanoskaalas toimuvaid vastastikmõjusid. Nende protsesside uurimiseks sobib väga hästi helihargi tüüpi kvartsresonator (QTF). Seadme tundlikkus on piisav nanoskaalas toimuvate muutuste mõõtmiseks. QTF on läbivaks uurimisvahendiks kõikides doktoritöö raames teostatud eksperimentaalsetes töödes, mille lühikirjeldus toodud allpool

Töötati välja meetod, mis võimaldas elektronmikroskoobi sees reaallajas kontrollitavalt positsioneerida siledal pinnal Au nanoosakesi ja ZnO nanotraate koos mehaaniliste omaduste väljaselgitamisega mõõtes samaaegselt hõõrdejõude.

Jõusensori valmistamiseks kinntati kvartsresonaatori (QTF) ühele haarale aatomijõu mikroskoobi (AFM) teravik. Mõõtmisi teostati kahes erinevas võnkeriigis: risti ja paralleelselt pinnaga. Paralleelse võnkeriigi korral leiti, et sensor omab suuremat tundlikkust ja võimaldab tulemuste otsest tõlgendust.

Pinnaga ristvõnkumise korral on lihtsam tagada teraviku ja pinna vahelauguse konstantsus, kuid samas lisandub tundmatu ja eksperimendis arvestamata jääv vertikaalne jõukomponent, mis suurendab mõõtmiste määramatust.

Kasutades seda mõõtemetoodikat leiti seosed nanoosakeste kuju ja hõõrdeomaduste vahel. Leiti ka termilise töötlemise mõju kulla nanoosakeste kujule ja hõõrdeomadustele.

Nanotraatide (NW) hõõrdeomaduste väljaselgitamiseks paigutati positsioneeriv teravik NW keskele ja lohistati mööda siledat alust. Young'i mooduli leidmiseks, mis kasutakse ka NW hõõrdejõude arvutamiseks, paigutati NW fokuseeritud ionkiirega (FIB) söövitatud „kaeviku” ühele äärele nõnda, et pool NW paiknes vabalt üle ääre augu kohal, mis võimaldas teda painutada kalibreeritud AFM teravikuga ja seeläbi ka määrata vastav paindele mõjuv jõud. See meetod vähendab hõõrdumise mõõtmiste määramatust, kuna iga NW Young'i moodul mõõdetakse eraldi konkreetse traadi jaoks ja ei ole vaja kasutada materjali keskmistatud Young'i moodulit. Selles mõõteprotsessis pole vajadust kasutada liimimist ega keevitust, seega säilivad nanotraadid ja nende omadused ning nad on ka järgmistes eksperimentides korduvkasutatavad. Mõõtmistes kasutati erineva pikkuseja ja läbimõõduga nanotraate ning näidati lineaarset seost traadi läbimõõdu ja hõõrdejõudu vahel

Lisaks eksperimentaalsetele mõõtmistele uuriti nanoosakeste omadusi teoreetilise modelleerimise kaudu. Töötati välja uus pingeleevendus mehhanismi mudel viisnurksete nanoosakete ja- varraste jaoks. Leiti, et nanovarrastel ja

nanoosakestel mittekattuva võrestruktuuriga pinnakihti moodustumine võiks vähendada osakeste siseenergiat. Teoreetiliselt määrati ka optimaalsed võreparametrite erinevused, millega kaasneks maksimaalne energia vabanemine. Leiti minimaalne raadius, et vastava kattekihi moodustumine oleks energeetiliselt eelistatud, mis on umbes 10 nm nanoosakeste ja 100 nm nanovarraste jaoks.

Eksperimentaalsete tulemuste usaldusväärsuse tõstmiseks töötati välja unikaalne meetod AFM teraviku puhastamiseks eksperimendi käigus. Ainulaadne tehnoloogia võimaldab AFM teravikku puhastada ilma uuritavalt kohalt liikumata. Meetodis kasutatakse puhastusvahendina süsihappegaasi, mis kondenseeritakse uuritavale objektile lume kujul. CO₂-lumel on abrasiivsed omadused ja skanneerides teravikuga üle “lumise” uuritava pinna saaste eemaldub. Pärast puhastusprotsessi on võimalik jätkata mõõtmisprotsessi objektil täpselt samast kohast. Meetod on patenteeritud.

Kasutades QTF-i töötati välja uus meetod ja vastav seade aineosakeste adsorptsioonikineetika jälgimiseks vesilahuses. Sensor koosneb süsiniknanotorudest valmistatud nanopoorsest fiibrist, mis on kinnitatud kvartsresonaatori ühele haarale. Meetodil on eeliseid teiste tuntud andurite kasutamise ees, ja samas on lahendatud QTF kasutamisega vesilahustes seotud probleemid. Väljatöötatud meetod on patenteeritud. Leiutise rakendatavust biosensoorikas näidati valgu (Bovin Serum Albumin) adsorptsioonikiiruse määramisega süsinikust nanotorufiibri pinnale erinevatel pH (pH 7 ja pH 4.8) väärtustel.

Tulemuste uudsus

Esmakordselt kasutati helihargi tüüpi kvartsresonatori baasil valmistatud jõesensorit millega manipuleeriti kulla nanoosakesi koos samaaegse hõõrdejõu mõõtmistega. Seejuures võrreldi rist- ja parrallelvõnkereziimide iseärasusi ja sobivust nanostruktuuride manipuleerimiseks ja nanotriboloogilisteks uuringuteks.

Leiti kulla nanoosakeste morfoloogia ja hõõrdejõudude vahelised seosed, kontrollitavalt manipuleerides neid oksüdeeritud räni pinnal elektronmikroskoobi sees. Demonstreeriti kulla osakeste kuju muutust ja staatilise hõõrdumise vähenemist pärast termilist töötlemist, mis oli oluliselt väiksem kulla sulamistemperatuurist.

Töötati välja originaalne meetod ühe ja sama nanotraadi elastsus- ja hõõrdeomaduste väljaselgitamiseks realajas.

Töötati välja viisnurksete nanoosakeste ja nanovarraste pingeelenduse uudne mudel, mis baseerub alusega mittekattuva võreparameetriga pinnakihi tekkel. Arvutati optimaalsed parameetrid, millega kaasneks maksimaalne energia vabanemine.

Töötati välja uudne *in situ* aatomijõu mikroskoobi teraviku puhastusmeetod, mis põhineb CO₂-e lume abrasiivsetel omadustel ning millega kaob vajadus muuta teraviku asendit proovi kohal.

Töötati välja uudne meetod ja vastav seade, mis võimaldab reaajas jälgida adsorptsioonikineetikat vesilahuses. Mõõdeti valgu adsorptsioonikiirust süsinikust nanotorufiibri pinnale erinevatel pH väärtustel.

REFERENCES

- ¹ Friedt J. M. and Carry É., Introduction to the quartz tuning fork, *Am. J. Phys.*, **Vol. 75**, No. 5, (2007)
- ² X. D. Su, C. C. Dai, J. Zhang and S. O'Shea, Quartz tuning fork biosensor. *Biosens. Bioelectron.* **17** (2002)
- ³ J. Zhang, S. O'Shea, Tuning forks as micromechanical mass sensitive sensors for bio- or liquid detection, *Sens. Actuators B* **94** 65–72 (2003)
- ⁴ S. J. O'Shea, M. E. Welland, Atomic force microscopy at solid–liquid interface, *Langmuir* **14** 4186 (1998)
- ⁵ J. Rychen: Combined Low-Temperature Scanning Probe Microscopy and Magneto-Transport Experiments for the Local Investigation of Mesoscopic Systems. *Swiss Federal Institute of Technology*, Diss. ETH No. **14119** (2001).
- ⁶ A. Arnau, T. Sogorb, and Y. Jimenez. A continuous motional series resonant frequency monitoring circuit and a new method of determining butterworth-van dyke parameters of a quartz crystal microbalance in fluid media. *Rev. Sci. Instr.*, **71**(6):2563–2571, (2000).
- ⁷ Y. Tomikawa, H. Miura, and S. B. Dong. Analysis of electrical equivalent circuit elements of piezo tuning forks by the finite element method. *IEEE Trans. Sonics Ultrason.*, **SU-25**(4):206–212 (1978).
- ⁸ J. Rychen, T. Ihn, P. Studerus, A. Herrmann, K. Ensslin, H. J. Hug, P. J. A. van Schendel, and H. J. Guntherodt. Operation characteristics of piezoelectric quartz tuning forks in high magnetic fields at liquid helium temperatures. *Rev. Sci. Instr.*, **71** (3) (2000)
- ⁹ D. Zeisel, H. Menzi, L. Ullrich, A precise and robust quartz sensor based on tuning fork technology for (SF₆)-gas density control, *Sens. Actuators A80* 233 (2000)
- ¹⁰ Z. Lin, C. M. Yip, I. S. Joseph, M. D. Ward, Operation of an ultrasensitive 30 MHz QCM in liquids, *Anal. Chem.* **65** 1546 (1993)
- ¹¹ L. F. Matsiev, J. W. Bennett, E. W. McFarland, *IEEE ULTSYM* 459–462 (1998)
- ¹² X. Zhou, T. Jiang, J. Zhang, X. Wang and Z. Zhu, Humidity sensor based on quartz tuning fork coated with sol–gel-derived nanocrystalline zinc oxide thin film, *Sens. Actuators B* **123** 299–305 (2007)
- ¹³ J. Zhang C. Dai, X. Su, S. O'Shea, *Sens. Actuators B* **84** 123–128 (2002)
- ¹⁴ Binning, G., Quate, C. F., Gerber, C. H., Atomic Force Microscope. *Phys. Rev. Lett.*, **56** (9) 930–933 (1986).
- ¹⁵ Robert D. Grober, Jason Acimovic, Jim Schuck, Dan Hessman, Peter J. Kindelmann, Joao Mespanha, A. Stephen Morse, Khaled Karrai, Ingo Tiemann, and Stephan Manus. Fundamental limits to force detection using quartz tuning forks. *Rev. Sci. Instr.*, **71**(7):2776–2780 (2000).
- ¹⁶ T. R. Albrecht, P. Grutter, D. Horne, and D. Rugar. Frequency modulation detection using high-q cantilevers for enhanced force microscope sensitivity. *J. Appl. Phys.*, **69**(2):668–673 (1991).
- ¹⁷ D. Sarid, Scanning Force Microscopy with Applications to Electric, Magnetic and Atomic Forces. *New York: Oxford University Press* (1994).
- ¹⁸ C.J. Roberts, M.C. Davies, S.J.B. Tendler and P.M. Williams, Scanning Probe Microscopy, Applications, *Encyclopedia of Spectroscopy and Spectrometry (Second Edition)*, 2473–2480, Elsevier Ltd. (1999)
- ¹⁹ Hong-Qiang Li, The Common AFM Modes,
<http://www.chembio.uoguelph.ca/educmat/chm729/afm/details.htm>, (1997)

- ²⁰ J. R. Smith, An Overview to Scanning Probe Microscopy, *Educ. Chem.*, **34**(4) 107–111 (1997)
- ²¹ P. Gunther, U. Ch. Fischer, and K. Dransfeld. Scanning near-field acoustic microscopy. *Applied Physics B*, 48:8992, (1989)
- ²² K. Karrai and Robert Grober. Piezoelectric tip-sample distance control for near field optical microscopes. *Appl. Phys. Lett.*, **66** (14):1842–1844, (1995)
- ²³ A. G. Ruiter, J. A. Veerman, K. O. van der Werf, and N. F. van Hulst. Dynamic behavior of tuning fork shear-force feedback. *Appl. Phys. Lett.*, **71** (1):2830 (1997)
- ²⁴ K. Karrai and I. Tiemann. Interfacial shear force microscopy. *Phys. Rev. B*, **62** (19):13174–13181 (2000)
- ²⁵ H. Edwards, L. Taylor, W. Duncan, and A. J. Melmed. Fast, high-resolution atomic force microscopy using a quartz tuning fork as actuator and sensor. *J. Appl. Phys.*, **82**(3):980–984 (1997)
- ²⁶ W. H. J. Rensen and N. F. van Hulst. Atomic steps with tuning fork based noncontact atomic force microscopy. *Appl. Phys. Lett.*, **75** (11):1640–1642 (1999)
- ²⁷ F. J. Giessibl. High-speed force sensor for force microscopy and profilometry utilizing a quartz tuning fork. *Appl. Phys. Lett.*, **73**(26):3956–3958, (1998)
- ²⁸ J. Rychen, T. Ihn, P. Studerus, A. Herrmann, K. Ensslin, H. J. Hug, P. J. A. van Schendel, and H. J. Guntherodt. Force-distance studies with piezoelectric tuning forks below 4.2k. *Appl. Surf. Sci.*, **157**(4):290–294 (2000)
- ²⁹ S. Rozhok, V. Chandrasekhar, *Solid State Commun.* **121** 683–686 (2002)
- ³⁰ O. Boldenkov, Probes and Cantilevers for SPM, umasch, www.spmtips.com/bibliography/probes_and_cantilevers
- ³¹ A. Kuhle, A. Zandbergen, J.B. & Bohr, Contrast artefacts in tapping tip atomic force microscopy. *Appl. Phys. A* **66** 329–332 (1998)
- ³² B. Neves, M. Salamon, Observation of topography inversion in atomic force microscopy of self-assembled monolayers. *Nanotechnology* **10** 399–405 (1999)
- ³³ M. Tomitori, T. Arai, Tip cleaning and sharpening processes for noncontact atomic force microscope in ultrahigh vacuum. *Surf. Sci.* **140** 432–438 (1999)
- ³⁴ M. Fujihira, Y. Okabe, Y. Tani, M. Furugori, U. Akiba, A novel cleaning method of gold-coated atomic force microscope tips for their chemical modification. *Ultramicroscopy* **82** 181–191 (2000)
- ³⁵ T. Nakagawa, M. Soga, New method for fabricating a mixed monolayer using self-assembly of trichlorosilanes and mapping of different molecules in the mixed monolayer using a frictional force microscopy with a tip chemically modified with fluoroalkyltrichlorosilanes for chemical sensing. *Jpn J Appl Phys* **36** 5226–5232 (1997)
- ³⁶ Tsukruk, V., Bliznyuk, V, Adhesive and friction forces between chemically modified silicon and silicon nitride surfaces. *Langmuir* **14**, 446–455 (1998)
- ³⁷ Y.-S. Lo, N. Chan, W. Dryden, P. Hagenhoff, Organical and inorganical contamination on commercial AFM cantilevers. *Langmuir* **15**, 6522–6526 (1999)
- ³⁸ G. Lee, D. Kidwell, R. Colton, Sensing discrete streptavidin biotin interactions with atomic-force microscopy. *Langmuir* **10**, 354–357 (1994)
- ³⁹ C. Pereira de Souza, M. S. Andrade, B. Neves, Microsc. Implementation of Recycling Routes for Scanning Probe Microscopy Tips. *Microanal.* **8**, 509–517 (2002)
- ⁴⁰ S. Ghandi, VLSI Fabrication Principles: Silicon & Gallium Arsenide. *New York: John Wiley & Sons, Inc* (1994)

- 41 J. P. Spatz, S. Sheiko, M. Möller, Shape and quality control of modified scanning force microscopy tips, *Ultramicroscopy* **75** 1–4 (1998)
- 42 C. Costa, E. Radovanovic, E. Teixeira-Neto, M.C. Goncalvec, F. Galembeck, A Procedure for SPM Tip Recovery, *ACTA MICROSCOPICA* **12** (2003)
- 43 C. Tolkendorf, I. Revenko, Choosing AFM Probes for Biological Applications, *Veeco Application Notes* (2004)
- 44 E. Gnecco, R. Bennewitz, O. Pfeiffer, A. Socoliuc, and E. Meyer, "Friction and wear on the atomic scale", *Springer Handbook of Nanotechnology*, B. Bhushan, ed., Springer, (2004)
- 45 H. Ahmed, *J. Vac. Sci. Technol.* **B 15** 2101 (1997)
- 46 B. Anczykowski, B. Gotsmann, H. Fuchs, J. P. Cleveland, V. B. Elings, *Appl. Surf. Sci.* **140**, 376 (1999)
- 47 S. Kim, D. C. Ratchford, X. Li, *ACS Nano* **3** 2989–2994 (2009)
- 48 C. Baur, A. Bugacov, B. E. Koel, A. Madhukar, N. Montoya, T. R. Ramachandran, A. A. G. Requicha, R. Resch, P. Will, *Nanotechnology* **9** 360 (1998)
- 49 D. Dietzel, M. Feldmann, H. Fuchs, U. Schwarz, A. Schirmeisen, *Appl. Phys. Lett.* **95** 053104 (2009)
- 50 M. Sitti, H. Hashimoto, *IEEE-ASME Trans. Mech.* **5** 199–211 (2000)
- 51 D. Dietzel, T. Mönninghoff, L. Jansen, H. Fuchs, C. Ritter, U. Schwarz, A. Schirmeisen, *J. Appl. Phys.* **102** 084306 (2007)
- 52 Y. Xia, P. Yang, Y. Sun, Y. Wu, B. Mayers, B. Gates, Y. Yin, F. Kim and H. Yan, One-dimensional nanostructures: synthesis, characterization, and applications, *Adv. Mater.* **15** 353–389 (2003)
- 53 Z. L. Wang, R. P. Gao, P. Poncharal, W. A. de Heer, Z. R. Dai and Z. W. Pan, Mechanical and electrostatic properties of carbon nanotubes and nanowires, *Mater. Sci. Eng. C* **16** 3–10 (2001)
- 54 Zhang Z., Qiu M., Andersson U., Tong L., "Subwavelength-diameter silica wire for light in-coupling to silicon-based waveguide", *Chin. Opt. Lett.* **5** 577–579 (2007)
- 55 S. K. Lee, H. J. Choi, P. Pauzauskie, P. Yang, N. K. Cho, H.-D. Park, E. K. Suh, K. Y. Lim and H. J. Lee, *Phys. Status Solidi C: Conf.* **1** 2775–2778 (2004)
- 56 A. Kolmakov, Y. Zhang, G. Cheng, M. Moskovits, *Adv. Mater.* **15** 997–1000 (2003)
- 57 L. Samuelson, M. Bjork, K. Deppert, M. Larsson, B. Ohlsson, N. Panev, A. Persson, N. Skold, C. Thelander, L. Wallenberg, *Physica E* **21** 560–567 (2004)
- 58 C. Soci, A. Zhang, B. Xiang, S. Dayeh, D. Aplin, J. Park, X. Bao, Y. H. Lo, D. Wang, *Nano Lett.* **7** 1003–1009 (2007)
- 59 M. Gudiksen, L. Lauhon, J. Wang, D. Smith, C. Lieber, *Nature* **415** 617–620 (2002)
- 60 K. Ziegler, D. Lyons, J. Holmes, D. Erts, B. Polyakov, H. Olin, K. Svensson, E. Olsson, *Appl. Phys. Lett.* **84** 4074–4076 (2004)
- 61 Z. Wang, *Adv. Funct. Mater.* **18** 3553–3567 (2008)
- 62 K. Liu, P. Gao, Z. Xu, X. Bai, E. Wang, *Appl. Phys. Lett.* **92** 213105 (2008)
- 63 S. Ramanathan, S. Patibandla, S. Bandyopadhyay, J.D. Edwards, J. Anderson, *J. Mater. Sci.: Mater. Electron* **17**, 651 (2006)
- 64 Jr H. He, Cheng L. Hsin, Jin Liu, Lih J. Chen, and Zhong L. Wang, Piezoelectric Gated Diode of a Single ZnO Nanowire, *Adv. Mater* **19**, 781–784 (2007)
- 65 Wang, H. T.; Kang, B. S.; Ren, F.; Tien, L. C.; Sadik, P. W.; Norton, D. P.; Pearton, S. J.; Lin, J. "Hydrogen-selective sensing at room temperature with ZnO nanorods". *App. Phys. Lett.* **86**: 243503 (2005)

- ⁶⁶ J. Salvétat, J. Bonard, N. Thomson, A. Kulik, L. Forro, W. Benoit, L. Zuppiroli, *Appl. Phys. A* **69** 255–260 (1999)
- ⁶⁷ L. Ngo, D. Almecija, J. Sader, B. Daly, N. Petkov, J. Holmes, D. Erts, J. Boland, *Nano Lett.* **6** 2964–2968 (2006)
- ⁶⁸ E. Wong, P. Sheehan, C. Lieber, *Science* **277** 1971–1975 (1997)
- ⁶⁹ Y. Huang, X. Bai, Y. Zhang, *J. Phys.: Condens. Matter.* **18** L179–L184 (2006)
- ⁷⁰ M. Manoharan, A. Desai, G. Neely, M. Haque, *J. Nanomater.* 849745 (2008)
- ⁷¹ M. Yu, B. Files, S. Arepalli, R. Ruoff, *Phys. Rev. Lett.* **84** 5552–5555 (2000)
- ⁷² Y. Zhu, F. Xu, Q. Qin, W. Fung, W. Lu, *Nano Lett.* **9** 3934–3939 (2009)
- ⁷³ C. Hsin, W. Mai, Y. Gu, Y. Gao, C. Huang, Y. Liu, L. Chen, Z. Wang, *Adv. Mater.* **20** 3919–3923 (2008)
- ⁷⁴ C. Lin, H. Ni, X. Wang, M. Chang, Y. Chao, J. Deka, X. Li, *Small* **6** 927–931 (2010)
- ⁷⁵ R. Agrawal, B. Peng, H. Espinosa, *Nano Lett.* **9** 4177–4183 (2009)
- ⁷⁶ A. Lugstein, M. Steinmair, A. Steiger, H. Kosina, E. Bertagnolli, *Nano Lett.* **10** 3204–3208 (2010)
- ⁷⁷ S. Barth, C. Harnagea, S. Mathur, F. Rosei, *Nanotechnology* **20** 115705 (2009)
- ⁷⁸ M. Manoharan, M. Haque, *J. Phys. D: Appl. Phys.* **42** 095304 (2009)
- ⁷⁹ G. Conache, S. Gray, A. Ribayrol, L. Froberg, L. Samuelson, H. Pettersson, L. Montelius, *Small* **5** 203–207 (2009)
- ⁸⁰ S. Ino, *J. Phys. Soc. Jpn.* **21** (1966) 346
- ⁸¹ C. Cleveland and U. Landman, *J. Chem. Phys.* **94**, 7379 (1991)
- ⁸² I. L. Garzo'n, K. Michaelian, and J. M. Soler, *Phys. Rev. Lett.* **81**, 1600 (1998)
- ⁸³ V. G. Gryaznov, A. M. Kaprelov, A. E. Romanov, and I. A. Polonskii, *Phys. Status Solidi B* **167**, 441 (1991)
- ⁸⁴ A. E. Romanov, I. A. Polonsky, V. G. Gryaznov, S. A. Nepijko, T. Junghanns, and N. I. Vitrykhouski, *J. Cryst. Growth* **129**, 691 (1993)
- ⁸⁵ J. Farges, M. de Feraudy, B. Raoult, and J. Torchech, *Surf. Sci.* **106**, 95 (1981)
- ⁸⁶ J. Uppenbrink and D. J. Wales, *J. Chem. Phys.* **96**, 8520 (1992)
- ⁸⁷ U. Landman, T. G. Schaaff, M. N. Shafigullin, P. W. Stephent, and R. L. Whetten, *Phys. Rev. Lett.* **79**, 1873 (1997)
- ⁸⁸ M. José Yacamán, J. A. Ascencio, H. B. Liu, and J. Gardea-Torresdey, Structure shape and stability of nanometric sized particles, *J. Vac. Sci. Technol.* **B** **19**, 1091 (2001)
- ⁸⁹ C. Gutierrez-Wing, P. Santiago, J. A. Ascencio, A. Camacho, and M. Jose'-Yacama'n, *Appl. Phys. A: Mater. Sci. Process.* **70**, 1 (2000)
- ⁹⁰ S. Ijima and H. Ichihashi, *Phys. Rev. Lett.* **56**, 616 (1986)
- ⁹¹ P. Williams, *Appl. Phys. Lett.* **50**, 1760 (1987)
- ⁹² L. D. Marks, *Rep. Prog. Phys.* **57**, 603 (1994)
- ⁹³ T. Ben-David, Y. Lereach, G. Deustcher, J. M. Penisson, A. Bourret, R. Kofman, and P. Cheyssac, *Phys. Rev. Lett.* **78** 2585 (1997)
- ⁹⁴ H. Zhang, J. Tang, P. Zhu, J. Ma, L. Qin, *Chem. Phys. Lett.* **478**, 230–233 (2009)
- ⁹⁵ D. Golberg, Y. Bando, W. Han, K. Kurashima, T. Sato, *Chem. Phys. Lett.* **308** 337 (1999)
- ⁹⁶ L. E. Valenti, P. A. Fiorito, C. D. Garcia, C. E. Giacomelli, *J. Colloid Interface Sci.* **307** 349–356 (2007)
- ⁹⁷ J. Tang, B. Gao, H. Geng, O. D. Velev, L. Qin, O. Zhou, *Adv. Mater.* **15** 1352–1354 (2003)
- ⁹⁸ A. J. Melmed, *J. Vac. Sci. Technol.* **B** **9** 601 (1991)

- 99 C. T. Gibson, G. S. Watson, S. Myhra, *Nanotechnology* **7** 259–262 (1996)
- 100 S.M. Cook, T.E. Schaffer, K.M. Chynoweth, M. Wigton, R.W. Simmonds, K.M.
Lang, *Nanotechnology* **17** 2135–2145 (2006)
- 101 J. Dietrich, *Pure Appl. Geophys.* **116** 790–806 (1978)
- 102 D. Dietzel, C. Ritter, T. Monninghoff, H. Fuchs, A. Schirmeisen, U. D. Schwarz,
Phys. Rev. Lett. **101** 125505 (2008)
- 103 D. Seo, C. I. Yoo, I. S. Chung, S. M. Park, S. Ryu, H. Song, *J. Phys. Chem. C* **112**
2469–2475 (2008)
- 104 R. W. Carpick, M. Salmeron, *Chem. Rev.* **97** 1163–1194 (1997)
- 105 K. L. Johnson, K. Kendall, A. D. Roberts, *Proc. R. Soc. A*, 324 301–313 (1971)
- 106 D. Maugis, *J. Colloid Interface Sci.* **150** 243–269 (1992)
- 107 D. Tabor, *J. Colloid Interface Sci.* **58** 2–13 (1977)
- 108 S. P. Timoshenko, J. N. Goodier, *Theory of Elasticity*; McGraw-Hill: NewYork,
(1987)
- 109 A. H. Cottrell, *Dislocations and Plastic Flowing Crystals*; Oxford University Press:
Oxford, U. K., (1953)
- 110 R. Resch, C. Baur, A. Bugacov, B. E. Koel, A. Madhukar, A. A. G. Requicha and
P. Will, *Appl. Phys. A* **67** 265–271 (1998)
- 111 L. Landau, E. Lifshitz, *Theory of Elasticity*, volume 7, third ed., Butterworth-
Heinemann, Oxford, (1986)
- 112 J. Song, X. Wang, E. Riedo, Z. Wang, *Nano Lett.* **5** 1954–1958 (2005)
- 113 M. Huang, Y. Wu, H. Feick, N. Tran, E. Weber, P. Yang, *Adv. Mater.* **13** 113–116
(2001)
- 114 B. Polyakov, L. Dorogin, A. Lohmus, A. Romanov and R Lohmus, In situ mea-
surement of kinetic friction of ZnO nanowires inside a Scanning Electron Micro-
scope, submitted
- 115 Ritter C, Heyde M, Stegemann B, Rademann K, *Phys. Rev. B* **71** 085405 (2005)
- 116 B. Polyakov, L. Dorogin, A. Lohmus, A. Romanov and R Lohmus, In situ mea-
surement of kinetic friction of ZnO nanowires inside a Scanning Electron Micro-
scope, submitted
- 117 M. Bordag, A. Ribayrol, G. Conache, L. Froberg, S. Gray, L. Samuelson, L. Mon-
telius, H. Pettersson, *Small* **3** 1398–1401 (2007)
- 118 A. Desai, M. Haque, *Appl. Phys. Lett.* **90** 033102 (2007)
- 119 H. Hofmeister, *Cryst. Res. Technol.* **33**, 3 (1998)
- 120 D. Seo, C. I. Yoo, I. S. Chung, S. M. Park, S. Ryu, and S. Hyunjoon, *J. Phys.*
Chem. C **112**, 2469 (2008)
- 121 V. G. Gryaznov, J. Heidenreich, A. M. Kaprelov, S. A. Nepijko, A. E. Romanov,
and J. Urban, *Cryst. Res. Technol.* **34**, 1091 (1999)
- 122 M. J. Yacaman, J. A. Ascencio, H. B. Liu, and J. Gardea-Torresday, *J. Vac. Sci.*
Technol. B **19**, 1091 (2001)
- 123 V. G. Gryaznov, A. M. Kaprelov, A. E. Romanov, and I. A. Polonskii, *Phys. Stat.*
Sol. (b) **167**, 441 (1991)
- 124 Dorogin, L.; Vlassov, S.; Kolesnikova, A.; Kink, I.; Löhms, R.; Romanov, A.
Crystal mismatched layers in pentagonal nanorods and nanoparticles. *Physica*
Status Solidi B-Basic Solid State Physics, **247** (2), 288–298 (2010)
- 125 Dorogin, L.; Vlassov, S.; Kolesnikova, A.; Kink, I.; Löhms, R.; Romanov, A.
Pentagonal Nanorods and Nanoparticles with Mismatched Shell Layers. *Journal of*
Nanoscience and Nanotechnology, **10** (10), 6136–6143 (2010)

ACKNOWLEDGEMENTS

First of all I would like to express gratitude to my supervisor Rünno Lõhmus for involving and continuously supporting me in such an interesting research.

I want to thank all coauthors for pleasant teamwork. Special thanks go to Ants Lõhmus and Ilmar Kink for all kind of support and advising during all years of study in University of Tartu, to Boris Polyakov for being “unofficial” supervisor in nanomanipulation experiments and for constructive criticism of the thesis, to Leonid Dorogin and Alexey Romanov for providing essential theoretical support, to Kristjan Saal for supervising me in all chemistry connected activity, to Vambola Kisand for help on educational side and paperwork, and to all other colleagues.

Many thanks to Karine Mougin and Samer Darwich for warm welcome at Institut de Science des Matériaux de Mulhouse and for sharing the knowledge and experience in the field of nanotribology and nanoparticle synthesis.

I am also grateful to Madis Lobjakas and Fredrik Punga for technical assistance, to Siim Pikker for assistance with SEM, and to Stiina Kristal for language editing.

Warm thanks to my wife Elena and to my parents for their support and believe in me.

Work was supported by the Estonian Science Foundation grants no. 8428, 8377 and 8420; Estonian research targeted project SF0180058s07; Graduate School on Functional Materials and Technologies; EU Social Funds project 1.2.0401.09-0079; University of Tartu; Estonian Nanotechnology Competence Centre and by ESF FANAS program "Nanoparma".

PUBLICATIONS

CURRICULUM VITAE

Sergei Vlassov

Date and place of birth: 01.05.1980, Tartu, Estonia
Citizenship: Estonia
Address: University of Tartu, Institute of Physics, Riia 142, 51014, Tartu,
Estonia
Telephone: +372 5594 1841

Education

1987–1999 Tartu Annelinna Gymnasium
1999–2005 University of Tartu, baccalaureus scientiarum (BSc), material
science
2005–2007 University of Tartu, magister scientiarum (MSc), applied
physics
2007–2011 University of Tartu, PhD student, material science

Professional employment

2004–2006 laborant, IPUT, Laboratory of Physics of Nanostructures
2006– ... engineer, IPUT, Laboratory of Physics of Nanostructures

Professional development

2006 Winter school „Sliding dynamics: The physical and mechanical
viewpoints on friction.” (Valpré, Lyon, France 19–24
November 2006)
2009 PhD Winter School in Nano Tribology (Technical University of
Denmark)

Awards

1999 University of Tartu, Institute of Physics, student award

ELULOOKIRJELDUS

Sergei Vlassov

Üldandmed

Sünniaeg ja koht: 01.05.1980, Tartu, Eesti
Kodakonsus: Eesti
Kontaktandmed: Tartu Ülikooli Füüsika Instituut, Riia 142, 51014, Tartu,
Estonia
Tel: +372 55941841

Haridus

1987–1999	Tartu Annelinna Gümnaasium
1999–2005	Tartu Ülikool, BSc, materjaliteadus
2005–2007	Tartu Ülikool, MSc, rakendusfüüsika
2007–2011	Tartu Ülikool, doktorant, materjaliteadus

Teenuskäik

2004–2006	laborant, TÜFI, Madalate temperatuuride labor
2006–...	insener, TÜFI, Nanostruktuuride füüsika labor

Erialane enesetäiendus

2006	Talvekool „Sliding dynamics: The physical and mechanical viewpoints on friction.” (Valpré, Lyon, France 19–24 November 2006)
2009	Talvekool „PhD Winter School in Nano Tribology” (Technical University of Denmark)

Preemiad

1999	TÜFI tudengistipendium
------	------------------------

DISSERTATIONES SCIENTIAE MATERIALIS UNIVERSITATIS TARTUENSIS

1. **Martin Järvekülg.** Tubular microstructures by Hf-, Zr- and Ti-butoxide gel sheet rolling. Tartu, 2011, 112 p.